UNIVERSITAT POLITÈCNICA DE VALÈNCIA

UNIVERSITAT POLITÈCNICA DE VALÈNCIA

School of Industrial Engineering

Study of nanolithography methods for the controlled deposition of nanoparticles in photonic devices for sensing applications

End of Degree Project

Bachelor's Degree in Biomedical Engineering

AUTHOR: Montero Barriga, Luis

Tutor: Martínez Abietar, Alejandro José

Cotutor: Pinilla Cienfuegos, Elena

ACADEMIC YEAR: 2023/2024

AGRADECIMIENTOS

Quiero expresar mi agradecimiento en primer lugar a mis tutores Alejandro Martínez Abiétar y Elena Pinilla Cienfuegos quienes me han brindado la oportunidad de realizar el TFG con ellos y poder trabajar en el Centro de Tecnología Nanofotónica (NTC) con ellos.

En segundo lugar, me gustaría agradecer al doctorando Javier Abilio Redolat Querol quién siempre ha estado ahí para solucionarme cualquier duda o problema y ayudarme en varios procesos experimentales en los laboratorios. Además, me gustaría agradecer también al resto del personal del NTC quienes han hecho que la estancia en el centro durante estos meses sea cómoda, divertida y llevadera.

Por último, agradecer a mi familia que me han apoyado durante todo este proceso y han estado ahí para ayudarme con cualquier cosa. Y a mis amigos, con los que he compartido y opinado sobre todas las etapas del trabajo y el proceso realizado.

RESUMEN

La deposición controlada de nanopartículas (NPs) sobre nanoestructuras fotónicas permite la creación de dispositivos novedosos capaces de realizar un confinamiento extremo de la luz y mejorar la interacción entre la luz y la materia. Este es un avance crucial para desarrollar aplicaciones como *lab-on-chip* y biosensores, así como la química plasmónica a gran escala. Sin embargo, el posicionamiento de NPs individuales en dispositivos nanoestructurados es un desafío. Hasta la fecha, el posicionamiento de NPs individuales se puede obtener mediante impresión láser sobre vidrio o por microscopía de fuerza atómica (AFM), pero estos métodos son complejos, caros y lentos.

El objetivo de este trabajo es desarrollar diferentes enfoques para la colocación controlada de NPs en sistemas fotónicos, tanto en nanoestructuras individuales (como nanocavidades optomecánicas y guías de ondas) como en metasuperficies y sustratos transparentes de grandes áreas.

Las diversas metodologías combinarán métodos de *bottom-up* y de *top-down*, como *drop-casting* en nanoestructuras funcionalizadas, la colocación de NPs mediante láser basado en la técnica de pinzas ópticas, métodos de litografía blanda con sellos elastoméricos y la impresión por micro contacto.

Palabras clave: Nanotecnología; nanolitografía; fotónica integrada; biosensores; posicionamiento de nanopartículas; metasuperficie; nanopartículas (NPs), cavidades optomecánicas; espectrometría Raman; Microscopía de Fuerza Atómica (AFM); litografía blanda; ángulo de contacto; impresión por inyección de tinta.

RESUM

La deposició controlada de nanopartícules (NPs) sobre nanoestructures fotòniques permet la creació de dispositius innovadors capaços de realitzar un confinament extrem de la llum i millorar la interacció entre la llum i la matèria. Aquest és un avanç crucial per a desenvolupar aplicacions com *lab-on-chip* i biosensors, així com la química plasmónica a gran escala. No obstant això, el posicionament de NPs individuals en dispositius nanoestructurats és un desafiament. Fins ara, el posicionament de NPs individuals es pot obtindre mitjançant impressió làser sobre vidre o per microscòpia de força atòmica (AFM), però aquests mètodes són complexos, cars i lents.

L'objectiu d'aquest treball és desenvolupar diferents enfocaments per a la col·locació controlada de NPs en sistemes fotònics, tant en nanoestructures individuals (com nanocavitats optomecàniques i guies d'ones) com en metasuperfícies i substrats transparents de grans àrees.

Les diverses metodologies combinaran mètodes de *bottom-up* i de *top-down*, com *drop-casting* en nanoestructures funcionalitzades, la col·locació de NPs mitjançant làser basat en la tècnica de pinces òptiques, mètodes de litografia blana amb segells elastomèrics i la impressió per micro contacte.

Paraules clau: Nanotecnologia; nanolitografia; fotònica integrada; biosensors; posicionament de nanopartícules; metasuperfície; nanopartícules (NPs); cavitats optomecàniques; espectrometria Raman; Microscòpia de Força Atòmica (AFM); litografia suau; angle de contacte; impressió per injecció de tinta.

ABSTRACT

The controlled delivery of nanoparticles (NPs) onto photonic nanostructures allows for the creation of novel devices capable of extreme light confinement and enhanced light-matter interaction. This is a crucial step to develop applications such as lab-on-a-chip and biosensors, as well as large-scale plasmonic chemistry. However single positioning NPs on nanostructured devices is challenging. To date single NP positioning can be obtained via laser printing onto glass or by Atomic Force Microscopy (AFM) but these methods are complex, expensive and slow methods.

The aim of this work is to develop different approaches for the controlled positioning of nanoparticles (NPs) onto photonic systems in individual nanostructures (such as optomechanical nanocavities and waveguides) as well as in metasurface and large-area transparent substrates.

The diverse methodologies will combine bottom-up and top-down methods such as drop casting on functionalized nanostructures, positioning NPs via laser based on optical tweezers technique, soft-lithography methods by elastomeric stamps and micro-contact printing.

Keywords: Nanotechnology; nanolithography; integrated photonics; biosensors; nanoparticle positioning; metasurface; nanoparticles (NPs); optomechanical cavities; Raman spectrometry; Atomic Force Microscopy (AFM); soft lithography; contact angle; inkjet printing.

INDEX

ACRONYMS LIST

NPs	Nanoparticles
ODS	Sustainable Development Goals
APTES	(3-Aminopropyl) triethoxysilane
NTC	Nanophotonic Technology Center
SCO	Spin crossover
EBL	Electron Beam Lithography
OM	Optical Microscopy
PMMA	Poly (methyl methacrylate)
PDMS	Polydimethylsiloxane
AFM	Atomic Force Microscopy
REM	Replica Molding
PDMS	Polydimethylsiloxane
BF	Bright Field
DF	Dark Field
SERS	Surface-Enhanced Raman Spectroscopy
LS	Low Spin
HS	High Spin
HRFESEM	High Resolution Field Emission Scanning Electron Microscope
SEM	Scanning Electron Microscope
ICMOL	Instituto de Ciencia Molecular
IPA	Isopropanol

LIST OF FIGURES

LIST OF TABLES

LIST OF EQUATIONS

DISSERTATION

Study of nanolithography methods for the controlled deposition of nanoparticles in photonic devices for sensing applications

CHAPTER 1. INTRODUCTION

1.1. Introduction

The current work focuses on the investigation of three projects involving diverse lithography methods to achieve the controlled deposition of several types of nanoparticles (NPs) in photonic devices for sensing applications**. This research aims to highlight the significance of nanolithography to explore the wide range of available methods, and specifically focus on the three techniques used in this work**.

The **objectives** followed in each project are: the controlled positioning of single nanoparticle (NP) in optomechanical cavities via laser, the manufacture of a reconfigurable metasurface based in molecular NPs by soft lithography, and finally the positioning of individual $BaTiO_3$ NPs via inkjet printing.

The **structure of this document** is explained as follows:

First, the motivation, general objectives, and individual goals of each project will then be outlined, along with the chronology of the research over the past months. Then, the state-of-the-art lithography techniques will be presented, followed by an explanation of the most commonly used methods. Next, the specific techniques employed in this research will be discussed. This is followed by a chapter detailing the materials, equipment, and methodologies used in the experimental part of the three projects. Subsequently, the document is divided into three chapters, each dedicated to one project. Each chapter includes sections on results and discussion, as well as conclusions and future work to optimize the project devices. Finally, the Sustainable Development Goals related to the work are addressed, followed by a budget section.

1.2. Motivation and Objectives

The current research focus in the advancement of various nanolithography methods to facilitate the controlled NP deposition, with a specific interest on enhancing photonic sensing devices. Establishing the most suitable method for precise NP placement is crucial for optimizing the signal in photonic devices. Although, it is challenging due to numerous experimental parameters such as time, temperature, applied force, and substrate chemistry, three different approaches will be presented showing various cases of accurate NP deposition in different photonic devices.

Going deeper into the specific motivations and objectives of each project, the principal ideas and the expected outcomes of this work will be explained for each project.

PROJECT 1: **Nanoparticle transference onto optomechanical cavities via laser**. The goal of this project is the positioning of gold (Au) NPs in the center of optomechanical cavities, previously functionalized with (3-Aminopropyl) triethoxysilane (APTES) molecules, to improve its detection function. This project aims to study the interaction of light within the optomechanical cavities, both in the presence and lack of NPs. Exciting the optomechanical cavities with resonant frequencies, any changes in the resulting signal can indicate the presence of NPs. So, achieving the correct deposition of the NP, the signal can be enhanced. Despite its difficulties, this approach is significant for advancing sensing methodologies in the field of photonic devices.

- This project is made in collaboration with the plasmonics, optomechanics, and chiral photonics group led by Prof. Alejandro Martínez (NTC, UPV).

PROJECT 2: **Reconfigurable metasurfaces based on spin crossover (SCO) NPs via soft lithography.** The purpose of this project is the development of reconfigurable metasurfaces based on a hybrid structure of a polymer with embedded NPs. Metasurfaces are structured systems with series of unit elements of regular materials. Depending on the arrangement of these elements it is possible to modify surface properties, controlling the interaction of light and its parameters [1]. Conventional metasurfaces are static, resulting in fixed parameters of light interaction. This research tries to overcome this limitation by creating active metasurfaces capable of dynamically altering light interaction properties, even after fabrication [2]. This is made possible by incorporating SCO NPs which can induce changes in the geometrical and optical characteristics of grating metasurfaces. SCO NPs are specially interesting because, under certain external stimulus (such as pressure or temperature), their electronic configuration can be switched between two spin states that are accompanied with variations in the volume and optical (refractive index) properties.

- This project is made in collaboration with Dr. Elena Pinilla-Cienfuegos (NTC, UPV) PI of the project SURFING: Reconfigurable metasurfaces combining molecular and chalcogenide tunable materials. (PID2021-128442NA-I00).

PROJECT 3: **Controlled positioning of individual $BaTiO_3$ NPs in transparent flat substrates via inkjet printing.** Inkjet printing will be employed to fabricate periodic structures with $BaTiO_3$ NPs with a series of specific dimensions at nanometre-scale. This technique is chosen for its ability to achieve dropping the NPs in a specific area of a surface with high resolution. The objective of this project is therefore to produce periodic structures of $BaTiO_3$ NPs over flat and transparent substrates with nanometer-scale precision for the characterization of a femtosecond laser beam. Femtosecond laser pulses with few optical cycles are technically challenging to characterize accurately. This difficulty arises from the need to characterize the spectral phase over an extremely broad spectral bandwidth, which can span hundreds of nanometres (for instance, from 650 to 1000 nm). It is precisely this extensive bandwidth that allows the achievement of laser pulses with durations around 6 fs, which contain only a few cycles of the electric field oscillation. Characterizing the phase in combination with the

spectrum provides the temporal intensity distribution of the laser through a simple Fourier transform. Additionally, a further complication in the characterization is the potential variation in the spectral phase at different spatial positions of the laser beam, known as spatial chirp. For this reason, the interaction of the laser beam with nanometric particles has potential for this type of characterization.

- This project is made in collaboration with Dr. Javier Hernández-Rueda from the group of FÍSICA DEL LÁSER, ÓPTICA CUÁNTICA Y ÓPTICA NO LINEAL at Universidad Complutense de Madrid.

To conclude, each project is driven by specific motivations and objectives:

-Positioning NPs via laser: To investigate the impact of gold NPs on the light interaction within optomechanical cavities, enhancing photonic sensing devices.

- Soft lithography: To develop dynamic metasurfaces capable of adjusting light interaction properties using SCO NPs.

- Inkjet Printing: To fabricate NP structures with precise dimensions and spacing for applications requiring nanoscale control over NP deposition.

By optimizing these nanolithography methods, the research aims to advance the capabilities of photonic sensing devices, contributing to the development of innovative sensing methodologies in various research domains.

In order to accomplish the primary goals of the work, a series of objectives must be achieved. Moreover, it is indicated the estimated duration of each objective in Figure 1.

- O1: **Nanoparticle transference onto optomechanical cavities via laser.** This objective involves the following tasks:
  - T1.1 - Functionalization of the optomechanical cavities with APTES.
  - T1.2 - Deposition of gold NPs in the functionalized cavities.
  - T1.3 - Verification of the existence of gold NP onto the optomechanical cavities by dark field optical microscopy (OM).
  - T1.4 - Learning the operation of Raman spectrometer and OM. Structural characterization by Raman spectroscopy and OM. NP displacement by (Raman) laser.
- O2: **Reconfigurable metasurfaces based on spin crossover NPs via soft lithography.** This objective involves the following tasks:
  - T2.1 - Preparing a polymeric matrix of Poly (methyl methacrylate) (PMMA) solution for the metasurface and the Polydimethylsiloxane (PDMS) for the stamps.
  - T2.2 - Fabrication of PMMA metasurfaces on Au substrates with the PMDS stamps by soft lithography methods.
  - T2.3 - Learning the operation of Atomic Force Microscopy (AFM).
  - T2.4 - Fabrication of PMMA layers with spin coating.
  - T2.5 - Fabrication of reconfigurable metasurfaces (hybrid PMMA+SCO NPs) and characterization of NPs SCO by Raman and AFM.
- O3: **Controlled positioning of individual $BaTiO_3$ NPs in transparent flat substrates via inkjet printing.** This objective involves the following tasks:

- T3.1 - To establish the parameters of the droplet deposition at the inject printing system with and without NPs.
- T3.2 - Preparation of different solutions of $BaTiO_3$ with ultrapure water.
- T3.3 - Localization of the NPs with OM and characterization by Raman spectroscopy.

O4: Study of the measurements, drafting, and revision of the document.

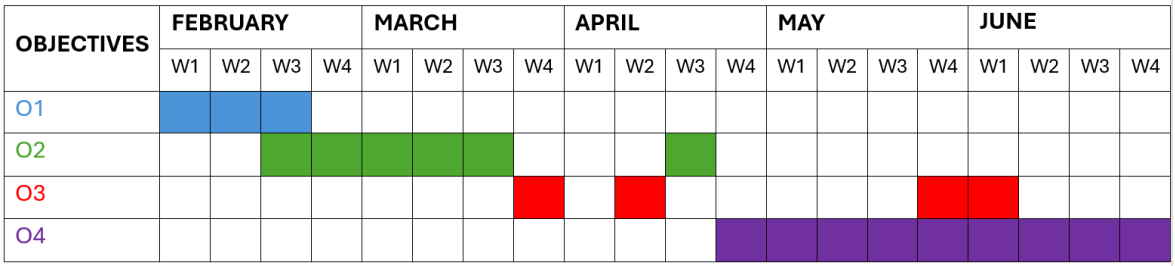

Figure 1: Chronology of the work.

1.3. State of the Art

Nanolithography is a crucial step to fabricate new devices in various fields such as photonics, biomedical sciences, biology, chemistry and telecommunications [3]. The easiest way to make precise nanostructures is by de use of traditional lithographs techniques like photolithography or electron beam lithography. However, these methods are expensive, slow and require specific machinery and infrastructure for their operation. Furthermore, sometimes they are not useful due to the specific features required for device fabrication such as the geometry or the chemical composition. Thus, there are other lithography techniques which are less expensive and faster. In this section conventional lithography methods as well as more specific nanolithography techniques will be presented.

The two predominant lithographic techniques utilized in contemporary fabrication processes are photolithography and electron beam lithography (EBL). Although these methods share similarities, they operate at distinct scales of fabrication due to inherent limitations imposed by the wavelength of the exposing radiation.

Photolithography is capable of managing dimensions as small as 1µm, leveraging the wavelength of UV light (350 – 430 nm) employed in its process [4]. Conversely, EBL surpasses this resolution, enabling the fabrication of nanostructures with lateral dimensions ranging from 20 to 30 nm [5].

Both techniques entail the assembly of a substrate with a thin film of dielectric or conductor, overlaid with a polymeric photoresist film. In the case of

photolithography, a photomask is utilized to generate a pattern on the photoresist. Once the pattern is transferred onto the polymer, it is replicated onto the underlying thin film. An illustration of the photolithography process is explained in Figure 1.

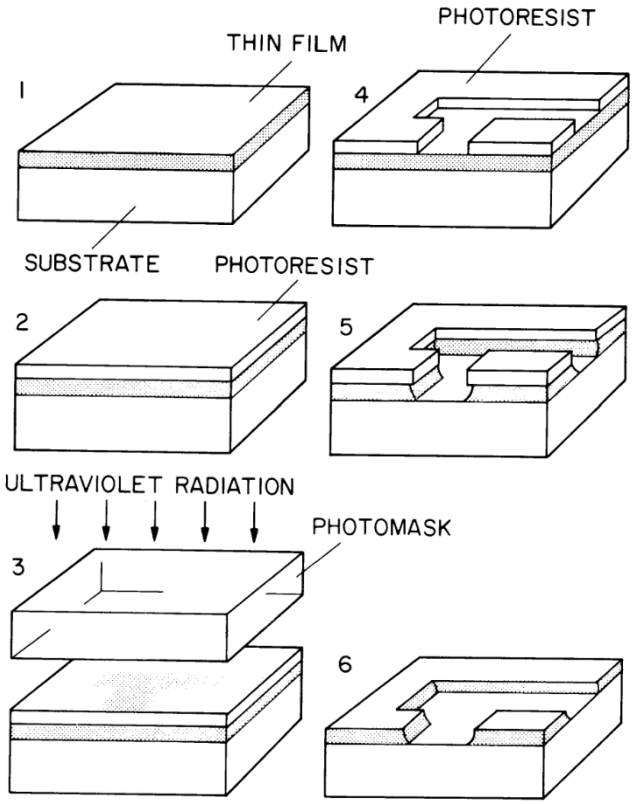

Figure 2: Explanation of the photolithography process from reference [4].

Both photolithography and electron beam lithography are suitable for the fabrication of micro-nanostructures, but they have several challenges. One significant inconvenience is the considerable amount of time and resources required for their design and implementation. Additionally, the high cost associated with the acquisition and maintenance of the necessary machinery and infrastructure is largely attributed to the requirement of conducting these processes within a clean room environment. Clean rooms are costly to construct and maintain at optimal conditions, further compounded by stringent access restrictions necessitating people to know specific protocols and safety measures.

Moreover, not all research facilities have clean room facilities. In such cases, outsourcing the fabrication of structures to institutions equipped with the requisite infrastructure becomes necessary, inevitably prolonging the overall process duration.

Furthermore, photolithography exhibits limitations when applied to non-planar substrates and lacks control over chemistry surface, which can impact the quality and uniformity of the fabricated structures.

Given these challenges, alternative lithographic methods offer faster sample production, greater convenience, and improved reproducibility. One such method is

soft lithography [5], which is highly effective for both micro and nano-scale fabrication. As previously mentioned, soft lithography offers rapid processing, enabling the production of multiple samples in a short timeframe, along with simplified procedures and cost-effective fabrication of diverse structures. Another powerful option is **inkjet printing** methodology that allows the precise and reproducible placement of NPs, enabling the creation of complex patterns and structures with high spatial resolution. It is a versatile, non-contact method that can be applied to a wide variety of substrates, including flexible and sensitive materials. Inkjet printing is also highly efficient, minimizing waste by using only the necessary amount of material. Additionally, it provides excellent control over the deposition process, allowing for the adjustment of parameters such as droplet size, deposition rate, and ink composition to achieve the desired properties of the NP films. This method is scalable and cost-effective, making it suitable for both research and industrial applications [6]. Finally, **optical tweezers** offer numerous advantages for trapping and manipulating molecules or nanoparticles (NPs) with high precision. This technique uses highly focused laser beams to exert piconewton-scale forces, allowing for the stable and non-invasive capture and manipulation of individual particles. Optical tweezers provide exceptional spatial control, enabling precise positioning and movement of NPs in three dimensions. This method is highly versatile, capable of handling a wide range of particle sizes and materials, including biological molecules and synthetic NPs. Additionally, optical tweezers can operate in various environments, such as liquid media, making them ideal for biological and chemical applications. The technique is also adaptable, allowing for the integration with other analytical tools like microscopy and spectroscopy, thus facilitating real-time observation and measurement of interactions at the nanoscale [7].

1.3.1. Soft lithography

The three principal techniques englobed by soft lithography are: microcontact printing (μCP), replica molding (REM), and solvent-assisted micromolding (SAMIM) [8]. While their initial steps are similar, each technique diverges in the patterning of the final thin film. For instance, it will be elaborated on the REM technique, which is the one employed in this research. However, it's important to note that all three techniques are rooted in molding, printing, and embossing processes.

In soft lithography, despite its advantages in speed and simplicity, there is one crucial step which demands significant time and costly resources: the fabrication of the master. This phase needs either photolithography or EBL, involving the comprehensive process outlined earlier [9].

Once the master is obtained, it serves as a template for creating a negative mold using a resin known as polydimethylsiloxane (PDMS). Upon curing, PDMS transforms into an elastomeric stamp, valued for its exceptional properties in micro and nanostructure fabrication. PDMS exhibits favourable characteristics such as ease of manipulation, adaptability to various surfaces, including microfluidic structures, and non-toxicity. Moreover, it has hydrophobicity with a contact angle of 110º and optical transparency [10].

Following the formation of the elastomeric stamp, the subsequent step involves imprinting the PDMS pattern onto a prepolymer, resulting in a replica of the master upon solidification induced by liquid evaporation. Figure 3 illustrates the four primary steps involved in soft lithography.

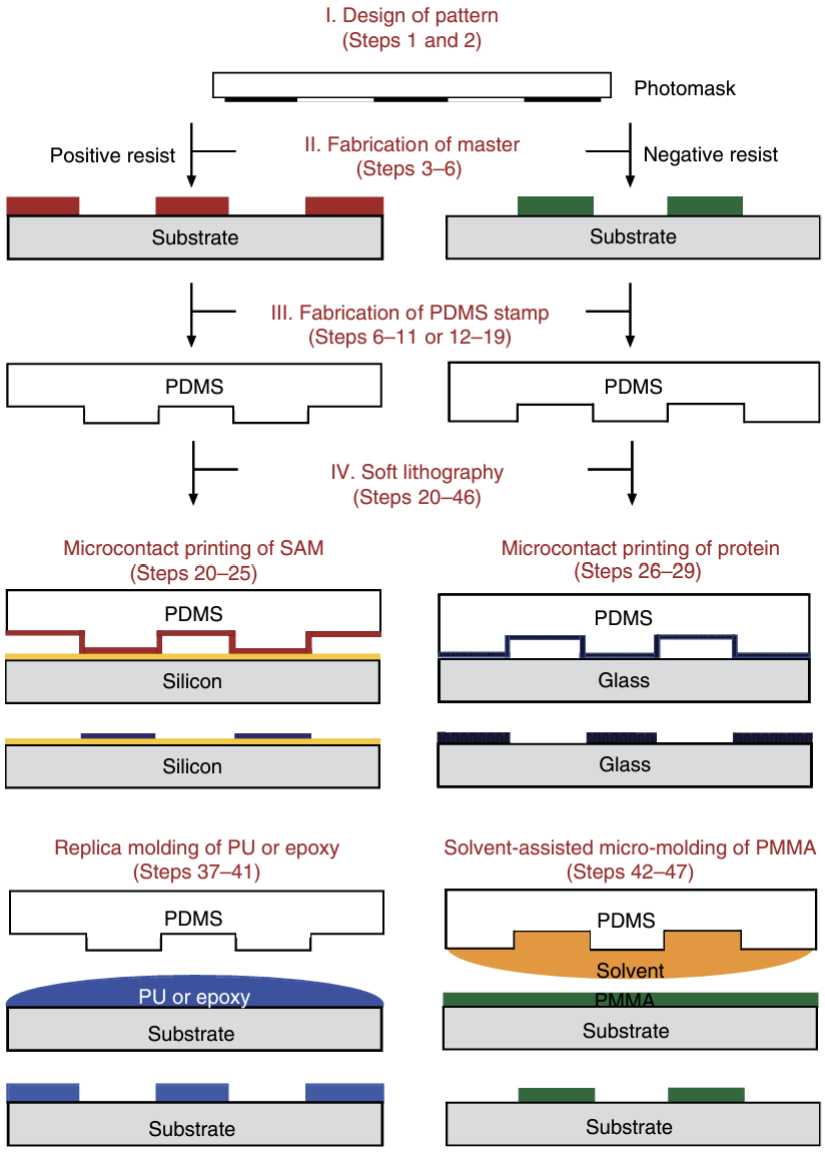

Figure 3: Schematic illustration of the four major steps involved in soft lithography and three major soft lithographic techniques from reference [5].

With this method, it can be produced numerous replicas of the master on substrates such as gold, silicon, or other metals, with the potential for near-atomic level reproduction. Additionally, soft lithography offers versatility in material selection, enabling work with a wide range of polymers. This stands in contrast to EBL, which typically requires a narrower selection of materials for effective processing.

1.3.2. Optical tweezers

Optical tweezers are used for trapping and manipulating molecules or NPs with high precision. This method enables researchers to conduct a variety of studies on NPs and is highly significant for numerous applications in nanotechnology, microbiology, photonics, and biomedical fields [7].

Optical tweezers manipulate NPs using lasers. The fundamental principles of this technique involve trapping NPs with two lasers aligned along the same axis but directed oppositely and using an additional laser to push the NP along an axis perpendicular to the initial one [11]. An example of this setup is shown in Figure 4.

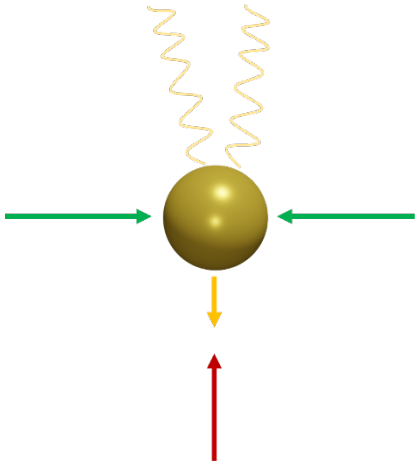

Figure 4: Optical tweezers performance.

This method is based on the excitation of the NP with the first two lasers. Since the lasers are directed oppositely, the NP remains stationary. When a third laser, perpendicular to the first two, de-excites the NP, it emits a photon, creating a traction force opposite to the direction of the photon which makes the NP has a recoil. Additionally, there are variations of optical tweezers that use plasmons to trap NPs. This technique excites a metallic surface to generate a surface plasmon, which can then be used to trap molecules [12] [11].

1.3.3. Inkjet printing

Another method for the controlled NP deposition is the inkjet printing, offering an improved alternative to drop-casting. Inkjet printing finds utility across a diverse array of fields, including biological applications, drug delivery, genomics, electrochemical sensors, mechanical manufacturing, and flexible electronics, among others [13]. One of its primary advantages lies in its precise material delivery at

nanoscale and picoscale levels, achieved through the controlled ejection of liquid droplets.

This technology also is high efficiency and cost-effectiveness due to its minimal material consumption, making it particularly advantageous when working with expensive, scarce, or toxic materials [14]. There are two main types of inkjet printing technologies: Continuous Inkjet Technology (CIJ) and Drop-on-Demand Inkjet Technology (DOD). We'll focus on the latter, as it is commonly used in the NTC (Nanophotonics Technology Center) and widely adopted in various applications.

Within the category of Drop-on-Demand (DOD) inkjet printing, there are three primary types distinguished by the mechanism used to eject ink: piezoelectric, thermal bubble, and electric power drives [15].

Piezoelectric inkjet printing relies on a piezoelectric element that undergoes deformation when subjected to external electric fields. This deformation results in the expulsion of ink droplets, which can be controlled by adjusting the pressure exerted by the piezoelectric element.

In thermal bubble inkjet technology employs an electric current to heat an element, generating bubbles within the ink. Controlling the volume of ejected ink poses a significant challenge, as it requires precise management of bubble size and direction through the heating process. Consequently, piezoelectric inkjet printing is often preferred due to its superior control and reliability in ink ejection.

Electronic inkjet printing involves applying a voltage pulse to an electrode, generating a force between the electrode and a vibrating plate. This deformation facilitates ink flow into the ink chamber, and when the voltage pulse ceases, ink is ejected.

Additionally, electrohydrodynamic jet printing technology represents an innovative approach, celebrated for its high resolution, adaptability to a wide range of ink viscosities, and ease in producing micro and nano-scale dots or lines. However, during ink ejection, drops are influenced by the distribution of the electric field. For further insights into the functionality, advantages, and limitations of this emerging technology, reference [15] provides an extended explanation.

Achieving optimal inkjet printing requires a thorough understanding and careful management of various parameters across four key aspects: printing equipment, ink composition, substrate properties, and printing technology.

The printing equipment plays a crucial role in determining both speed and resolution. For instance, reducing nozzle size can enhance resolution, but it also raises the risk of nozzle blockages. Other enhancements to speed and resolution are detailed in reference [15].

Ink composition significantly impacts printing quality. Properties such as electrical conductivity, pH value, viscosity, surface tension, and drop density influence the formation and deposition of ink droplets. Additionally, the occurrence of small satellite droplets after ejection and the coffee ring effect during deposition can

degrade print quality. Reference [15] provides detailed insights into optimizing these parameters.

Substrate properties also influence printing quality. The chemical and physical characteristics of the substrate can impact resolution. So, control over hydrophilicity and hydrophobicity can be critical factors on printing quality.

By carefully managing these parameters and understanding their interactions, researchers can optimize inkjet printing processes to achieve desired results efficiently and effectively.

CHAPTER 2. MATERIALS AND METHODOLOGY

This chapter will explain the materials and methodology used in the three research projects of the current work. First, the characterization and fabrication techniques will be presented. Second, the necessary materials for the projects will be described. Finally, the lithography methods used will be discussed.

2.1. Characterization Techniques

To analyse the results of the different studies, experimental measurements are required to provide information about the materials deposited on the substrate or the structure of the sample.

2.1.1. Atomic force microscopy (AFM)

AFM is a highly advanced scientific tool utilized for investigating surfaces at the nanoscale level. It employs a small flexible cantilever equipped with a sharp probe at its tip to meticulously scan the surface of a sample. As the probe interacts with the surface, it experiences subtle forces, which are precisely measured by monitoring the deflection of the cantilever. AFM enables researchers to surpass the diffraction limit, thereby facilitating the acquisition of high-resolution, three-dimensional images of the surface. Furthermore, AFM offers the capability of manipulating individual atoms and molecules. The information provided by AFM images includes the height of structures with nanometer-scale resolution. It is as the topography of the measured sample [16].

The AFM measurements were performed with an Alpha 300R system from WITec in AC mode (or tapping mode), where the cantilever tip lightly oscillates above the surface while scanning across it, with Sharp silicon probes (K∼42 N/m, f*0* ∼ 320 kHz) PPP-NCH (Nanosensors). AFM images were processed with WSxM software from Nanotec Electrónica S.L. [17].

2.1.2. Optical microscope (OM) in bright field (BF) and dark field (DF) modes

The OM utilizes visible light or other forms of electromagnetic radiation within the visible spectrum to examine and analyse samples, either at a macroscopic or microscopic scale. This method uses lenses and various optical components to amplify and discern details within the observed sample. By manipulating the interaction between light and matter using lenses, filters, and other optical devices, an enlarged and illuminated image of the sample is generated. This technique facilitates the investigation of sample morphology and structure, although its resolution is constrained by the diffraction limit, represented by $\Delta x = \lambda/(2^* NA)$, where Δx denotes resolution, λ represents the working wavelength, and NA is the numeric aperture of the optical system.

In BF microscopy, the sample is exposed to a strong light source, and the resulting image is created by the transmitted light that traverses through the sample.

DF microscopy is a modification of BF microscopy in which the sample is illuminated with oblique light. This technique collects only the scattered light from the different elements of the sample, showing structures such as NPs visible against a dark background. The diffracted light from the sample is predominantly produced by the NPs. Consequently, this phenomenon facilitates the identification of NPs more effectively than BF microscopy, particularly in samples with a high number of nanostructures.

The OM used is a Zeiss model, integrated into the WITec alpha 300 RA system, and features magnifications of 10x, 20x, 50x (with two focal distances: 9.1 mm and 0.5 mm) and 100x.

2.1.3. Raman spectrometer

To functionally characterize the SCO NPs in and out of the metasurfaces, a Raman spectrometer is employed. Additionally, the equipment incorporates an OM. The spectrometer operates at either 532 nm or 633 nm wavelengths, with adjustable power ranging from 0.1 mW to 26 mW. Moreover, the polarization of the beam can be modulated. The spectrometer captures the reflection anti-Stokes inelastic scattering, thus obtaining characteristic peaks of the Raman spectrum of the sensed molecule. Also, these measurements can be conducted on surfaces using Surface-Enhanced Raman Spectroscopy (SERS) substrates.

The Raman measurements were performed by a Spectrometer alpha300 RA (Raman-AFM) from WITec provides information about the AntiStokes Raman scattering in the 80 - 3000 cm^{-1} range, with monochromatic 532 nm (green) and 633 nm (red) laser illumination and 50x objective and 100x objective. Depending on the samples, the measurements were performed at different excitation wavelengths, with different powers and different magnifications (50x or 100x). The Raman images were scanned at different points per line and with different integration time at each point.

2.1.4. Scanning electron microscope (SEM)

High Resolution Field Emission Scanning Electron Microscope (HRFESEM) was utilized for characterizing the integration of the SCO NPs onto the PMMA grating and check their spatial distribution. Samples were scanned with a ZEISS GeminiSEM 500 available at “servicio de microscopía de la UPV”. The SEM is a LEO 1520 system with a Gemini column. The acceleration voltage can be set from 200 V to 30 kV. The column is equipped with a Schottky field emission electron source. To check the composition of the hybrid PMMA/SCO samples energy-dispersive X-ray spectroscopy (EDX) included in the GeminiSEM™ 500 system, was used.

2.1.5. Contact angle

To confirm the successful functionalization process for the optomechanical cavities with the APTES monolayer, contact angle measurement is employed. This method involves placing a water droplet onto the sample and measure the angle formed between the liquid drop and the surface. The software used for the contact angle measurement is *DROPimage Pro*. In Figure 5 there is an example of how the drop should look like over a functionalized sample.

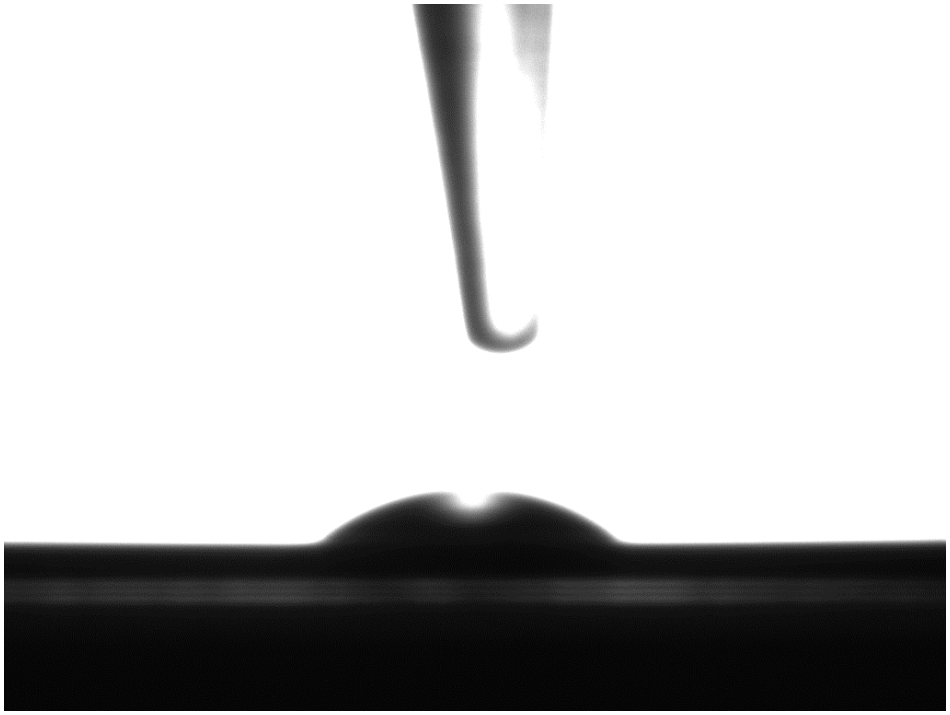

Figure 5: Image of the contact angle test.

The setup where is measured the angle are formed by a goniometer, a sample holder, and an automatic dispenser connected to a tip. The support is manually crafted, while the goniometer and dispenser are manufactured by Ramé-hart instrument company, a leading firm in surface science instruments [18]. In Figure 6 there is an image of the setup.

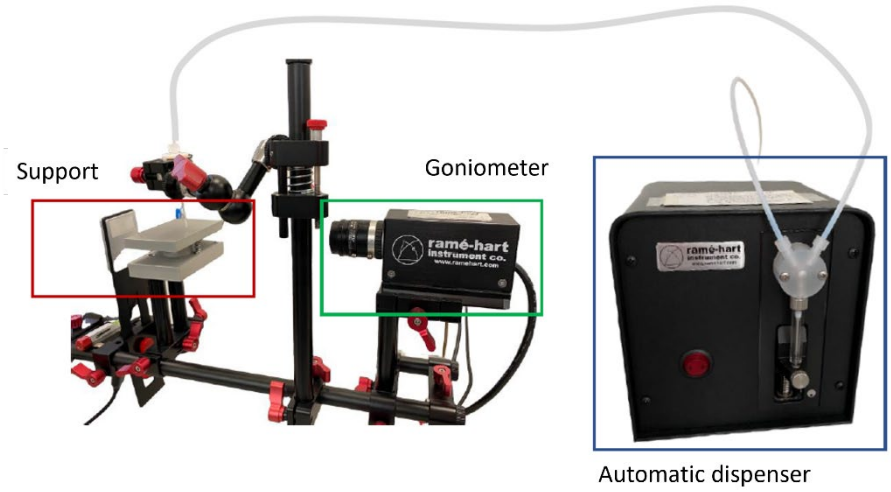

Figure 6: Contact angle setup.

2.2. Fabrication and Materials

To carry out all the experimental part it is necessary the fabrication of several items such as, substrates, PDMS master, and the use of different types of NPs and polymers. Some of them have a fabrication process or are involved in the experimental part of a project.

2.2.1. PDMS stamp manufacturing

The preparation of PDMS is done utilizing a commercial kit known as Silicon elastomer Sylgard 184 kit (Sygma Aldrich) composed by a base and a curing agent. The base and the curing agent are combined in a ratio of 10:1, respectively. Then, it is mix vigorously to ensure both agents are completely mixed. Due to the stirring process, air bubbles can be form, so if it is detected some bubbles, the mixture should be sonicated to eliminate them. When it is free of bubbles, it is cured in an oven at 90°C for 45 minutes. Following this duration, the PDMS is ready to be peeled of the master.

2.2.2. SCO NPs

The SCO NPs used in this work are NPs of chemical formula $Fe(NH_2Trz)_3(NO_3)_2$ surrounded by a silica shell of 1-2 nm (SCO@SiO_2 NPs) to confer chemical and mechanical stability. They present a rod like geometry (43 ± 9 nm length and 37 ± 9 nm width) with transition temperatures of 299 K (from Low Spin (LS) to High Spin (HS)) and 326 K (from HS to LS). They were synthesized with the method of reverse micelle made by the Instituto de Ciencia Molecular (ICMOL) [19]. The specific method to synthesize them are explained in the reference 19. These compounds are particularly interesting because, under certain external stimulus (such as pressure or temperature), their electronic configuration can be switched between two spin states (known as (LS) and (HS) states) [20]. The spin state transition produces variations in the volume, magnetic and optical (refractive index) properties, as well as in the electrical properties and colour (Figure 7).

Figure 7: Image at RT of the synthesized PMMA + SCO sample used in this work where it is visible the colour difference between de LS (pink) and HS (white) states. In collaboration with ICMol.

2.2.3. SCO NPs PMMA with SCO NPs solution

A diluted solution of polymethyl methacrylate (PMMA, Mw 350 000; Aldrich) in acetone (1.25% in weight) was mixed with SCO@SiO_2 NPs in a (1:1) ratio, using 5 mg of PMMA per 1 ml of acetone. Stirring is required as PMMA takes some time to dissolve, the SCO NPs and avoid agglomerations.

2.2.4. Au substrate fabrication

Chromium/gold (Cr/Au) thin films 5/80 nm thick were fabricated on silicon substrates using evaporation. The samples were cleaned with acetone, ethanol, and O_2 plasma before deposition. Cr/Au layers were fabricated at base vacuum pressure of 3.5 / 3.6 x 10^{-7} mbar and working pressure of 3.7 / 3.8 x 10^{-6} mbar using 8.5 / 9.5 KV High Voltage and 24 / 50 mA current. The rate of the deposited Au layers was controlled by a water-cooled quartz crystal monitor to be 1 Å/s. Mechanical profilometer Dektak 150 was used to assess the final thickness of 85 ± 4 nm.

2.2.5. Master fabrication

To create the PDMS stamp, a master mold was designed and fabricated on a Si substrate using a standard direct writing process based on e-beam lithography. The silicon master, comprising a periodic array of square wells, was produced using a conventional direct writing technique employing electron beam lithography. This fabrication process was conducted on standard silicon substrates (resistivity ρ ~1-*10* W.cm^{-1}, with a lightly p-doping of ~10*15* cm^{-3})

The procedure involved electron beam direct writing on a 100 nm Poly(methyl 2-methylpropenoate) (PMMA) resist film coated on the silicon substrates. Electron beam exposure, carried out using a Raith150 tool, was meticulously optimized to achieve the desired dimensions, utilizing an acceleration voltage of 10 KeV and an aperture size of 30 µm. Subsequently, the resist patterns were transferred onto the silicon substrates

using an optimized Inductively Coupled Plasma-Reactive Ion Etching (ICP-RIE) process employing fluoride gases such as SF6 and CF4.

To facilitate the separation of the PDMS stamp from the master, the master was coated with aluminium.

2.2.6. (3-Aminopropyl) triethoxysilane (APTES) functionalization

(3–Aminopropyl) triethoxysilane (APTES, 99%) molecules and solvents were purchased from Merck-Sigma Aldrich and used without previous purification. The functionalization involves the following steps.

First, beaker cleaning is performed twice using piranha solution (H_2SO_4/H_2O_2, 1:1). Then, APTES is extracted with a needle and syringe and stored in an Eppendorf. Next, with the sample cleaned by plasma, APTES functionalization is prepared by dipping the substrates in 4,4 µl of APTES with 20 ml of ethanol (absolute, reagent grade) for 45 minutes, then rinse with ethanol and finally dry under N_2 stream.

2.2.7. Au NPs deposited by drop casting

The drop casting was performed delivering a 10 µl drop of 150 nm Au-NP solution onto the functionalized optomechanical samples, left for 5 minutes and then rinsed with Mili-Q water, with a concentration of C = (2.3 ± 0.5) x 1010 particles/ml. Finally, the substrate was dried under N_2 stream. Water suspensions of spheric Citrate-capped 150 nm Au-NPs were purchased from BBI Solutions™.

2.2.8. NPs of BaTiO3 suspension preparation

Different suspensions of BaTiO3 NPs of 500nm (mg) in ultrapure water (ml) were prepared in 5 different concentrations: 0,05 : 1 – 0,2 : 1 – 0,33 : 1 – 0,5 : 1 – 1:1.

2.2.9. SiO2 substrate cleaning

Previously the drop cast of NPs, the Si substrates were cleaned with acetone and isopropanol (IPA). Then, the substrates were dried under N_2 stream. The size of the substrate was 24 x 24 mm and the thickness was 0,16 mm.

2.2.10.Inkjet printing procedure

To perform inkjet printing, a series of steps must be followed. The following is a summary of the startup process. Replace the water in the entire system with new ultrapure water. Open the SciFLEX_S3 program. Check and establish parameters such as centering the nozzle, voltage, pulse, velocity, drop shape, and its deviation. To print a drop, place the wells in the correct position and ensure the probe fits the selected well accurately. Figure 8 shows a representation of the wells' positions. Select the volume of the drop in picolitres (pl). Place the solution to be printed in a well and select

that well. Set the temperature and humidity. Finally, choose the drop distribution and start the run.

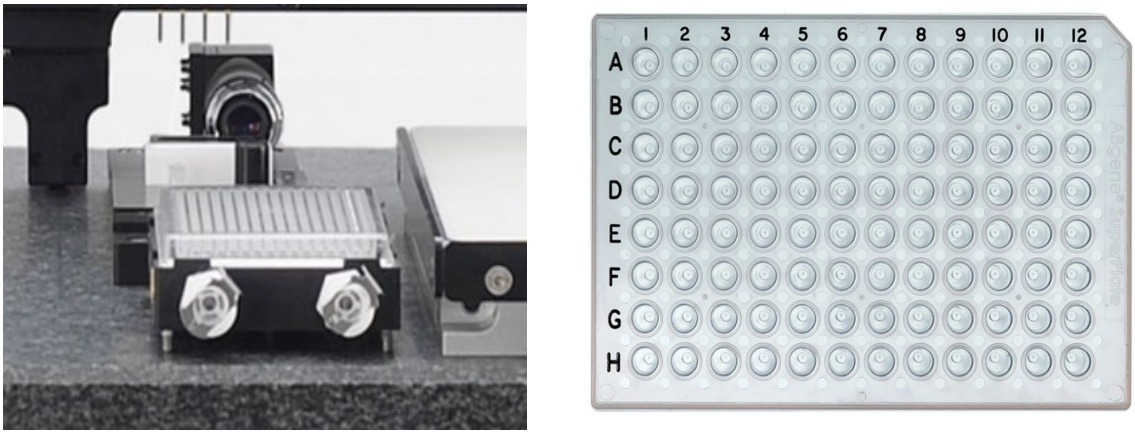

Figure 8: Image of the wells plate and their position.

There is a special maintenance process every 14 days. Connect the system to an ethanol 70 % filtered bottle for 20 minutes. Connect the system to an ultrapure water filtered bottle and let the system air out. In Figure 9 there is an image of the whole inkjet printer setup.

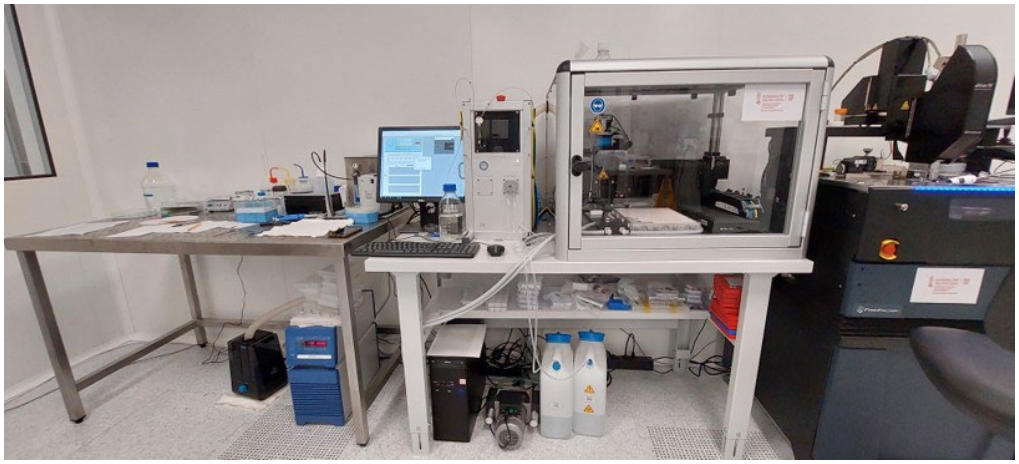

Figure 9: Setup of the inkjet printer.

CHAPTER 3. DEVELOPMENT OF HIGH ACCURACY SINGLE NANOPARTICLE POSITIONING VIA LASER IN OPTOMECHANICAL CAVITIES

3.1. Results and Discussion

3.1.1. Preparation of the optomechanical cavities

To prepare the sample with Au NPs, the functionalization with APTES molecules described previously was performed. This process is done due to APTES's affinity for silicon in the optomechanical cavity, where the silane group of APTES bonds with silicon, and its affinity for gold, where the amine group of APTES bonds with gold.

To verify successful functionalization, the contact angle test was used with the setup described in the materials and methodology section. A droplet of distilled water was placed outside the optomechanical cavities to avoid interference with the measurement. **A contact angle around 40º indicated proper functionalization**; if it was less than 40º, the functionalization process needed to be repeated. Figure 10 shows an example of the contact angle for a functionalized sample. Additionally, advancing and receding water contact angle measurements were performed to provide a more reliable dynamic average. Figure 11 presents these advanced receding water contact angle measurements.

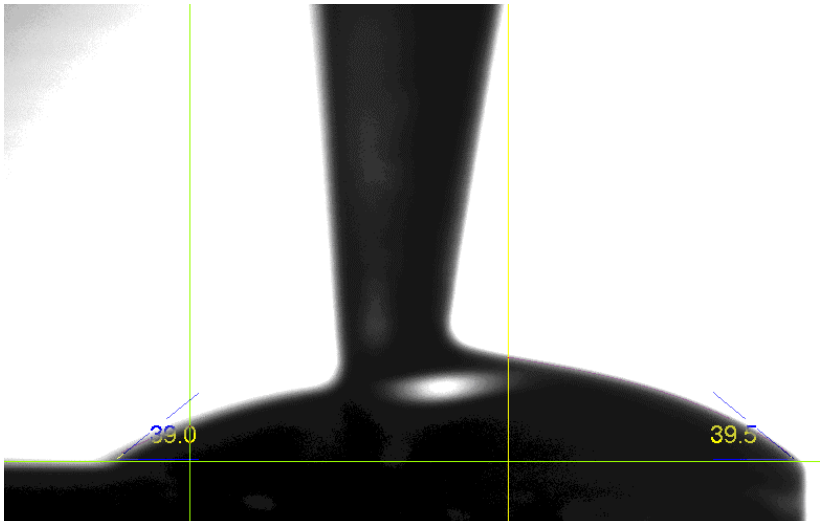

Figure 10: Contact angle of the optomechanical cavities functionalized with APTES monolayer.

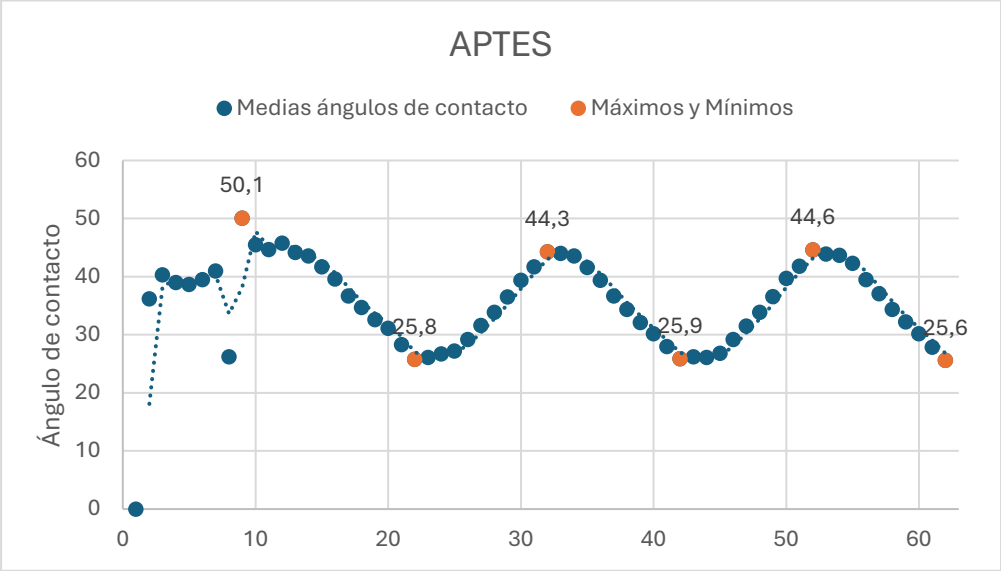

Figure 11: Advanced receding water contact angle measurements on the APTES functionalized optomechanical samples.

Immediately after to check if the functionalization was right, the Au NPs must be deposited in the optomechanical cavities. For this process there are steps to follow. Mix distilled water with HCl until the pH reaches 1, it is confirmed using specialized strips. Immerse the sample in the solution for 7 minutes. Then rinse it with ultrapure water and dry it with nitrogen gas. Finally, using a micropipette drop de Au NPs onto the sample, after 2 min rinse it with ultrapure water and dry it with nitrogen gas.

3.1.2. Characterization of the optomechanical cavities

To verify the deposition of Au NPs inside the optomechanical cavities, the sample was examined using an OM with DF located in the clean room. Observations under the DF revealed the presence of NPs within the optomechanical cavities, identifiable as small dots in the center. The size of these dots corresponded to the specified size of the Au NPs (150 nm). This conclusion was drawn based on the diffracted light produced by the NPs and by comparing the dot sizes to the dimensions of the optomechanical cavities, which measure 1570 nm at their widest part and 1070 nm at their narrowest part. Figure 12 shows an image of the optomechanical cavities with the Au NPs. Throughout the entire sample, a significant number of NPs were found inside the optomechanical cavities. This achievement is particularly important given the challenges of controlling NP placement using drop casting. In Figure 12 shown, 3 of the 12 optomechanical cavities contain Au NPs, representing a favourable ratio.

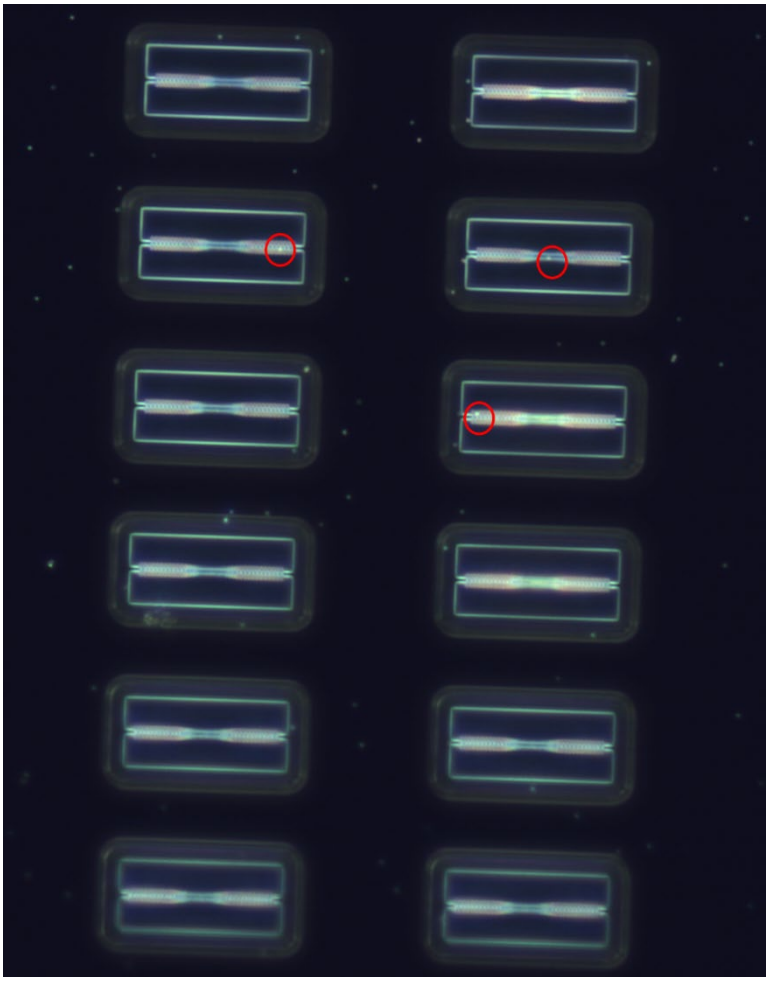

Figure 12: Optical image of an optomechanical cavities with Au NPs highlighted in red circles.

Once the optomechanical cavities with Au NPs were located using DF, they were analysed with a Raman spectrometer to confirm that the observed dots were indeed Au NPs. The presence of Au NPs would be indicated by a surface plasmon signal in the Raman spectrum. Most of the dots will show this characteristic surface plasmon signal, confirming their identity as Au NPs. However, some dots may be contaminants and don't present this signal.

To validate this approach, Raman spectra were initially obtained from individual Au NPs within the optomechanical cavities. However, these measurements predominantly showed peaks corresponding to silicon, as illustrated in Figure 13 B). Figure 13 A) shows the image of the measured point. Raman measurement was performed at 532 nm (green) excitation, P = 3,2 mW power, grating G = 600 l/mm and objective 100x. The single spectrum was scanned with 10 accumulations and with 1 s integration time per each accumulation.

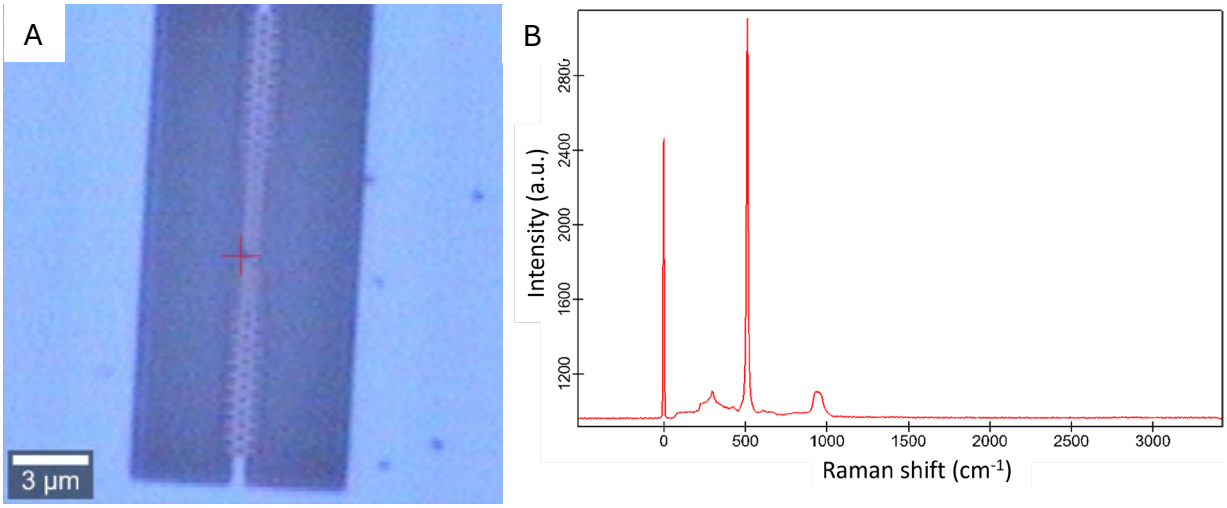

Figure 13: A) Optical image 100x of a NP onto an optomechanical cavity. B) Raman single spectrum of the cross shown in the image. Typical resonant peaks of the Silicon are present in the spectrum: 300 cm^{-1} TA-mode, 521 cm^{-1} crystalline Si mode and a broad peak around 900 cm^{-1} corresponding to the O-Si-O mode.

To examine a larger area and to obtain a signal of the Au NPs, an image scan was performed on some NPs located outside the optomechanical cavities, as indicated by the red square in Figure 14 A). The scan revealed the presence of two Au NPs, as shown in Figure 14 B), and the spectrum confirmed the existence of a surface plasmon, similar to the spectrum in Figure 14 C). This verified that the NPs were Au NPs. Raman measurement was performed at 532 nm (green) excitation, P = 3,2 mW power, grating G = 600 l/mm and objective 100x. The Raman images were a square of 10 µm x 10 µm, scanned at 80 points per line and 80 lines per image, with 0.1 s integration time at each point

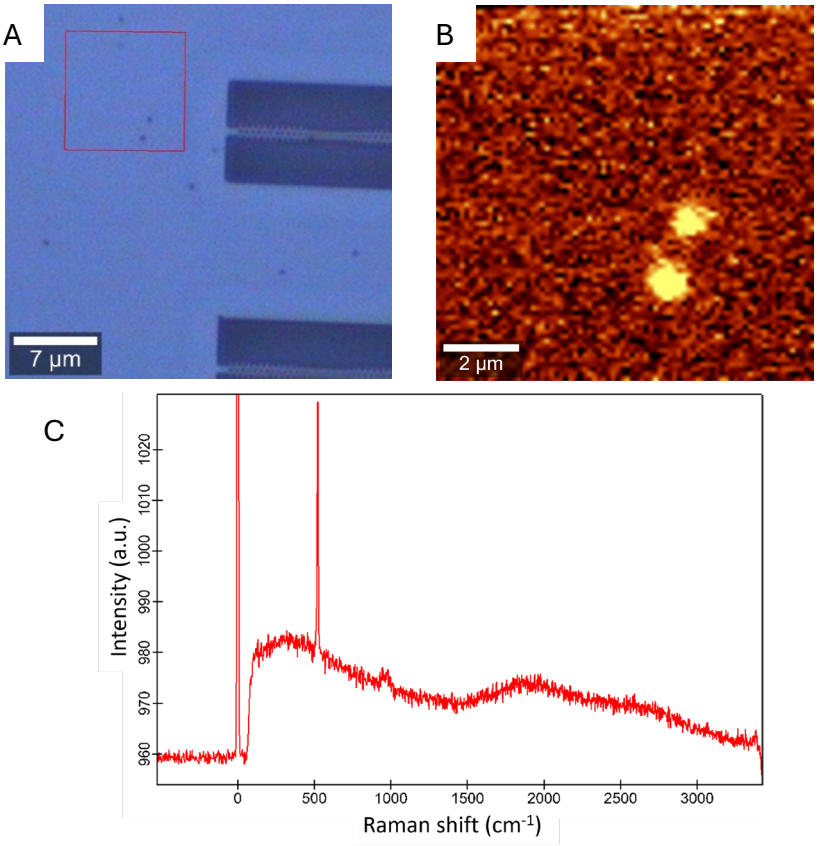

Figure 14: A) Optical image 100x of two NPs outside the optomechanical cavities. B) Raman image scan of the two NPs with a filter in 1450 cm^{-1}. C) Spectrum of an Au NP with a surface plasmon.

Once it was confirmed the dots were Au NPs, it was tried to make image scans of NPs onto the optomechanical cavities. Analysing the images scan, it was seen NPs on the waveguides forming the optomechanical cavities and on the gaps of the optomechanical cavities as it can be seen at Figure 15 A) and C). Also, the shape of the waveguide was represented clearly in the Figure 15 B) with a filter in 521 cm^{-1} (corresponding to changes in the peak intensity of the c-Si resonant peak), where it can even see black dots on the guide which represent the presence of Au NPs which also are seen like a bright spot in Figure 15 C where the APTES signal enhanced by the Au NPs is represented at 1450 cm^{-1}). Raman measurement was performed at 532 nm (green) excitation, P = 3,2 mW power, grating G = 600 l/mm and objective 100x. The Raman images were a square of 10 µm x 10 µm, scanned at 80 points per line and 80 lines per image, with 0.2 s integration time at each point.

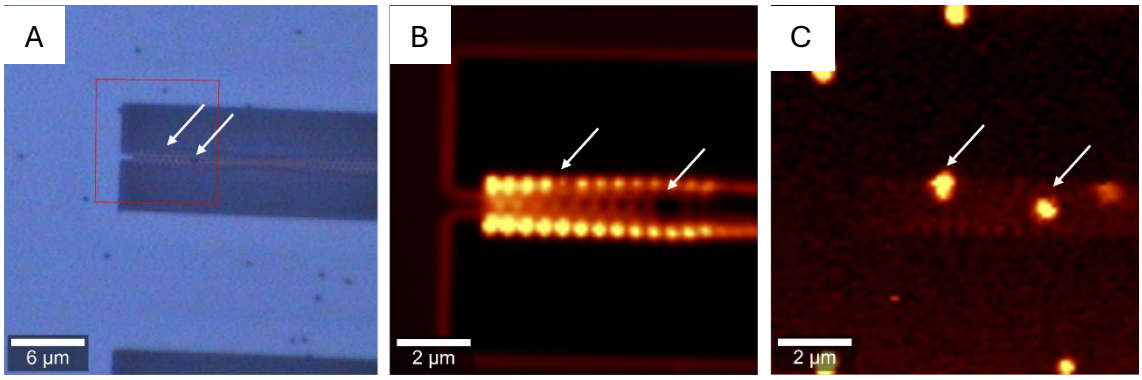

Figure 15: A) Optical image 100x of NPs onto an optomechanical cavity. B) Raman image scan of an optomechanical cavity with a filter in 521 cm^{-1}. C) Raman image scan of APTES (1450 cm^{-1}) where the Au NPs can be located thanks to the plasmonic enhancement.

The objective, after locating the NPs on the guide, was to move them to the center of the guide, where the signal measured for sensing applications is more optimal than at the sides of the optomechanical cavities. For this challenging task, it was tried to move one of the NPs using the optical tweezers technique. Unfortunately, the NTC does not possess optical tweezers technology, so it was tried to imitate its functionality using only one laser. Figure 16 shows the new configuration applied to move the NP.

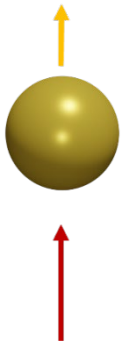

Figure 16: Functioning of moving an Au NP with one laser.

To move the Au NP with the laser, image scan was performed using a red laser (633 nm). This choice was based on Planck's Law, which states that shorter wavelength electromagnetic radiation produces higher energy in the electromagnetic radiation beam. Therefore, using the green laser (532 nm) would result in higher energy compared to the red laser. Consequently, by increasing the power of the green laser to move the NP would risk burning and destroying the optomechanical cavities.

$$E = h * v = \frac{h*c}{\lambda} \quad (1)$$

Equation 1: Planck's Law.

Thus, the red laser (633 nm) was used at maximum power to move the NP. The goal was to move the NP using the Raman in the direction of the scan (left to right). The area scanned is shown in Figure 17 A). The movement of the NP through the optomechanical cavity guide is shown in Figure 17 B) with a filter at 521 cm^{-1}(where the bright contrast indicates the presence of Silicon) appearing as a dark line (indicating the position of the moving Au NP) between two bright lines representing the Si waveguide. The movement of the Au NP is shown in Figure 17 C) with a filter at 1450 cm^{-1} (that represent the APTES signal enhanced by the Au NPs) appearing as a bright horizontal line in the middle of the image. Raman measurement was performed at 633 nm (red) excitation, P = 9,3 mW power, grating G = 600 l/mm and objective 100x. The Raman images were a square of 5 µm x 5 µm, scanned at 50 points per line and 50 lines per image, with 0.1 s integration time at each point.

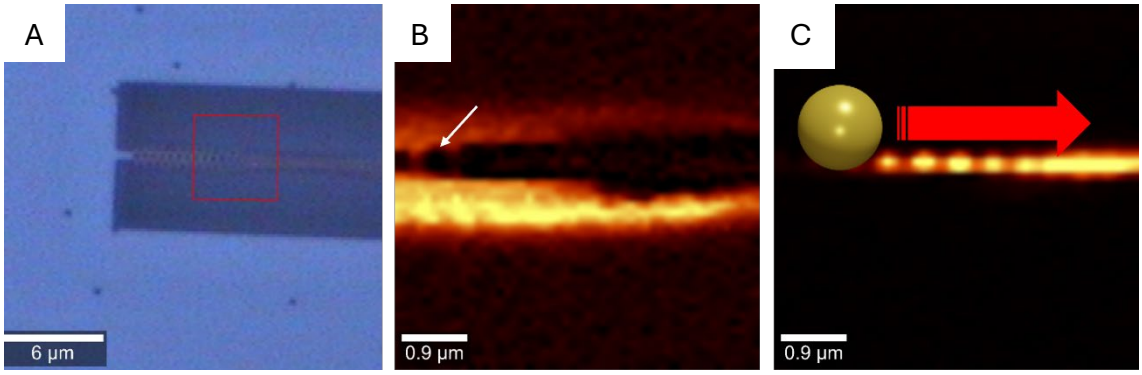

Figure 17: A) Optical image 100x of the square where there is the NP which is going to move. B) Raman image scan of the guide with the NP moving represented like a dark line with a filter in 521 cm^{-1}. C) Raman image scan of Au NPs movement with a filter in 1450 cm^{-1}.

To ensure the laser was not too powerful, a Raman image scan was performed using the green laser to analyse the structure of the optomechanical cavity. The scan revealed that the optomechanical cavity was destroyed, and the Au NP was below the guide, in the hollow created by the laser. Figure 18 A) shows the optomechanical cavity without a visible NP. The destroyed guide of the optomechanical cavity is shown in Figure 18 B) with a filter at 521 cm^{-1}. The NP is shown in Figure 18 C) with a filter at 1450 cm^{-1} as the brightest area, though with significant noise due to its position under the guide. Raman measurement was performed at 532 nm (green) excitation, P = 3,2 mW power, grating G = 600 l/mm and objective 100x. The Raman images were a square of 10 µm x 10 µm, scanned at 80 points per line and 80 lines per image, with 0,1 s integration time at each point.

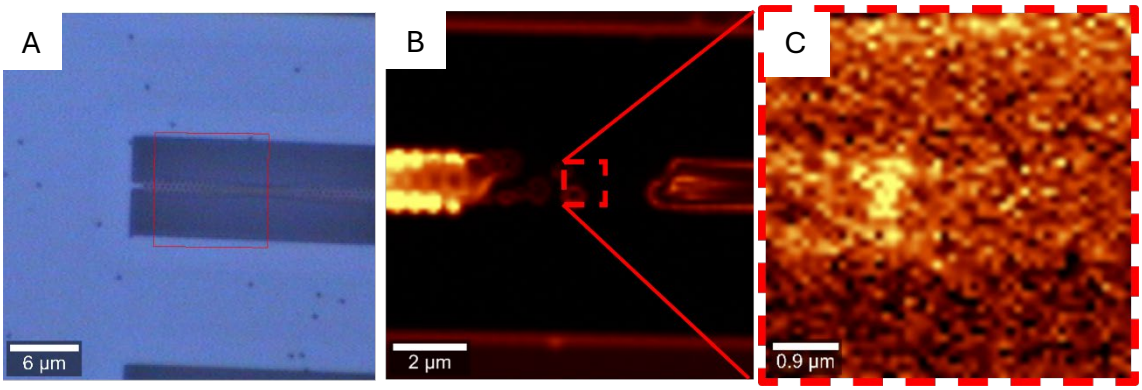

Figure 18: A) Optical image 100x of the square where there was the NP. B) Raman image scan of the guide destroyed with a filter at 521 cm^{-1}. C) Raman image scan of the Au NP with a filter in 1450 cm^{-1}.

Observing the destruction of the optomechanical cavity, it was concluded that the cause was the high laser power. Therefore, the next experiments will be conducted with reduced laser power to prevent burning and damaging the guide.

3.2. Conclusion and Future Work

To summarize, the first experimental attempt to move an Au NP was successful although the laser power must be optimized as well as the time of exposure to avoid the destruction of the Si optomechanical cavity. We think that this challenging new methodology for manipulating NPs with a laser will be improved in further experiments. Moreover, the preparation and characterization of the optomechanical cavities by Raman spectroscopy as well as the NPs characterization were successful.

First, the sample was functionalized with APTES to facilitate the subsequent deposition and localization of the Au NPs onto the optomechanical cavities. The contact angle test verified the functionalization was done correctly. Following this, Au NPs were deposited using the drop casting technique and characterized with dark field optical microscopy, which is more effective to localize NPs on the optomechanical cavity guides compared to bright field optical microscopy. Raman image scans were then performed, confirming that the black dots observed were Au NPs due to the surface plasmon generated in the Raman measurements.

Finally, it was concluded that the green laser delivered to much energy that burn the optomechanical cavities. However, using the red laser at maximum power we could move the NPs but finally it also destroyed the guides.

Throughout all the work developed so far, **it was achieved the principal objective which was placing NPs on the optomechanical cavities guides and move them via laser**. However, further work is needed to move the NPs to the center of the waveguide without damaging it. **Future work will focus on optimizing laser parameters and Raman image scan settings, such as power, scan geometry, integration time and the number of points and lines per image, to improve the precision of single NP positioning via laser**.

CHAPTER 4. MANUFACTURE OF RECONFIGURABLE METASURFACE BY SOFT LITHOGRAPHY

4.1. Results and Discussion

This chapter discusses the results of a reconfigurable metasurface fabrication made of a hybrid material of PMMA with SCO NPs by soft lithography methodology. As previously discussed, this lithography method involves the fabrication of soft stamps (PDMS in our case) and the transferred patterns over an ink (in our case PMMA with SCO NPs) in a flat surface. This work therefore involved three optimization processes: optimizing the master parameters (to fabricate the PDMS stamp), optimizing the PDMS stamps, and optimizing the pattern transferred to the sample to create the hybrid metasurfaces.

This section will explain the requirements and the experimental process for optimizing the master, the PDMS stamps, and the pattern transfer. The fabrication process for both kind of metasurfaces (PMMA and PMMA/SCO) followed the same steps except for the addition of the SCO NPs in the hybrid grating. 7 µL of the PMMA was drop cast onto the Au substrate using a micropipette, and the PDMS stamp was pressed on it following the procedure explained in in Figure 17.

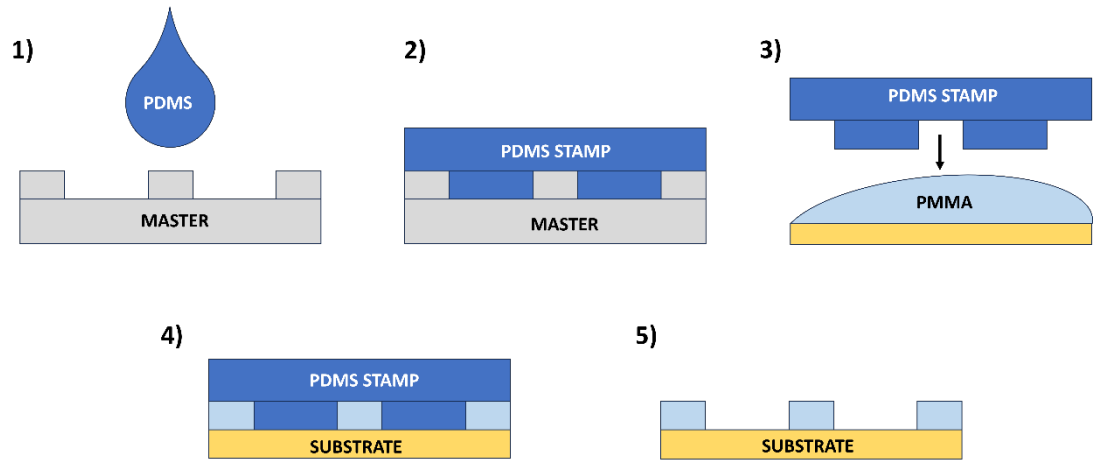

Figure 19: Metasurface fabrication process: 1) Freshly prepared PDMS is poured onto the master. 2) PDMS is cured in the oven for 45 minutes. 3) The PDMS stamp is released from the master mold. A 10 µl droplet of PMMA is deposited on an Au substrate. 4) The PMMA is then pressed under the PDMS seal with a controlled pressure. 5) Finally, the PDMS is withdrawn and the stamp print is transferred to the PMMA.

4.1.1. Master requirements

For fabricating the master, it was set some specifications about the grating pattern of the master get. In Figure 20 A) are shown the dimensions of the metasurface from which the master is fabricated. To optimize the master, it was made 4 grating patterns exactly the same as Figure 20 C). The size of the pattern is the 1mm per 1mm as is illustrated at Figure 20 B). In Figure 20 D) there is an image of the final master.

Finally, it was evaporated an aluminium layer on the master with the purpose of making easier to peel the PDMS stamps.

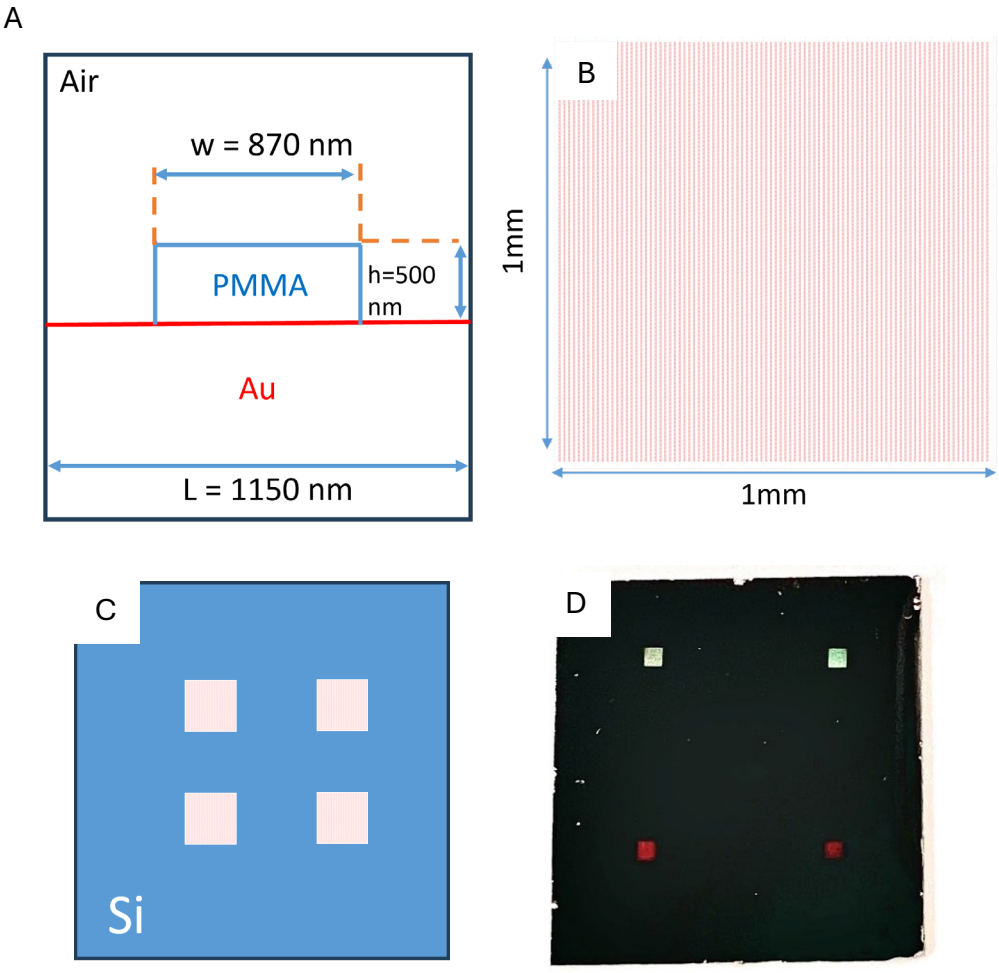

Figure 20: A) Scheme of the metasurface design, from which the master is fabricated. B) Bar scheme of the 1 x 1 mm ^{2}. C) Design of 4 replicas per Silicon substrate using e-beam lithography techniques. D) Image of the master made with the 4 replicas.

Once the PDMS were correctly peeled-off the Si mold, the quality and geometry of the stamps were characterized by high magnification optical microscopy (Figure 21 A)) and AFM microscopy (Figure 21 B) and C)). In Figure 21 B) and C) we represent AFM topography image and data profile of a PDMS stamp with the maximum patterning height transfer in this case was around 50-60 nm. However, AFM tip-convolution effects have to be taken into account that can limit the real depth of the patterns [21].

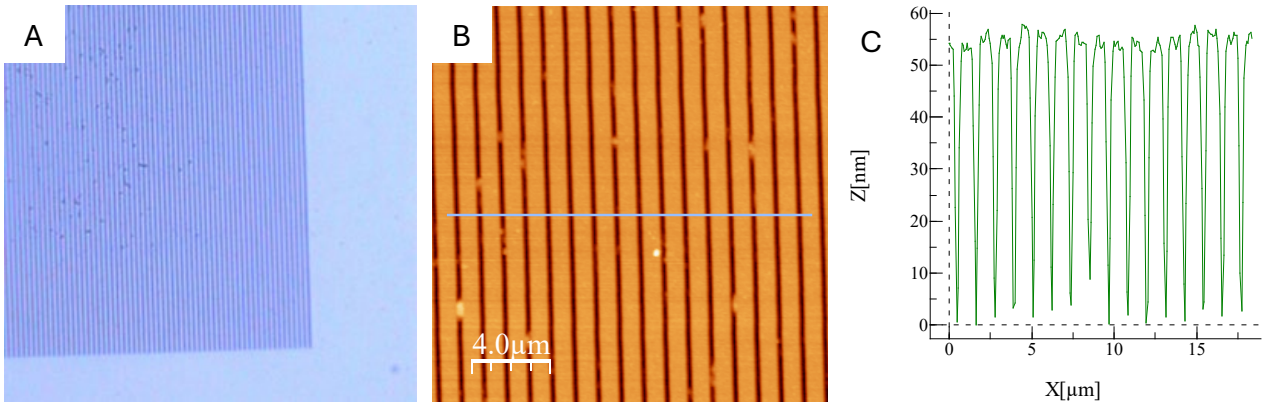

Figure 21: A) Optical image x20. B) AFM image of the master. C)AFM profile of the master.

4.1.2. PDMS stamps requirements and characterization

In order to fabricate high-quality PDMS stamps and metasurfaces, it was inevitable to produce multiple series of PDMS stamps and metasurfaces (or gratings) substrates. To determine the optimal features of PDMS stamps for achieving superior PMMA gratings height on the substrates, six series with four PDMS stamps in each series were made. It was studied the influence of the next parameters to optimize the PDMS stamps.

a) Firstly, the most suitable **thickness** was identified with the first fourth series. The first two series were very thin stamps, measuring less than 1 mm of thickness, making them easy to manipulate but prone to tearing during peeling. The third series was thicker at around 3 mm, proved more manageable for creating metasurface samples compared to the earlier series. However, it was a little bit more challenging for cutting with the cutter and subsequent peeling with tweezers than the previous series. Finally, within the fourth series, which had a thickness of 6 mm, it was determined that the optimal option was to produce stamps with a thickness of 3 mm. This decision was influenced by the difficulty encountered in cutting and peeling the stamps within the thicker series.

b) Another characteristic evaluated during the PDMS stamp fabrication process was the **curing time** in the oven. Typically, the curing duration was set at 45 minutes, but an experiment was conducted where the PDMS was cured for 90 minutes to enhance the stamps. However, it was observed that with the extended curing time, it became more challenging to cut the PDMS. Consequently, it was determined that waiting for the standard 45-minute duration produced better results.

c) Just as the curing time of PDMS was significant, the **timing of peeling the PDMS after its curing** was also crucial. Utilizing the OM, it was easy to discern the disparities between peeling the stamps on the same day as curing versus waiting until the following day. Peeling the stamps on the same day resulted in

irregularities and some fragments of the PDMS stamps adhering to the master. An example of a PDMS stamp peeled on the same day as curing is shown in Figure 22 A) next to its AFM image in Figure 22 B) where it is shown clearly the irregularities of the grating bars.

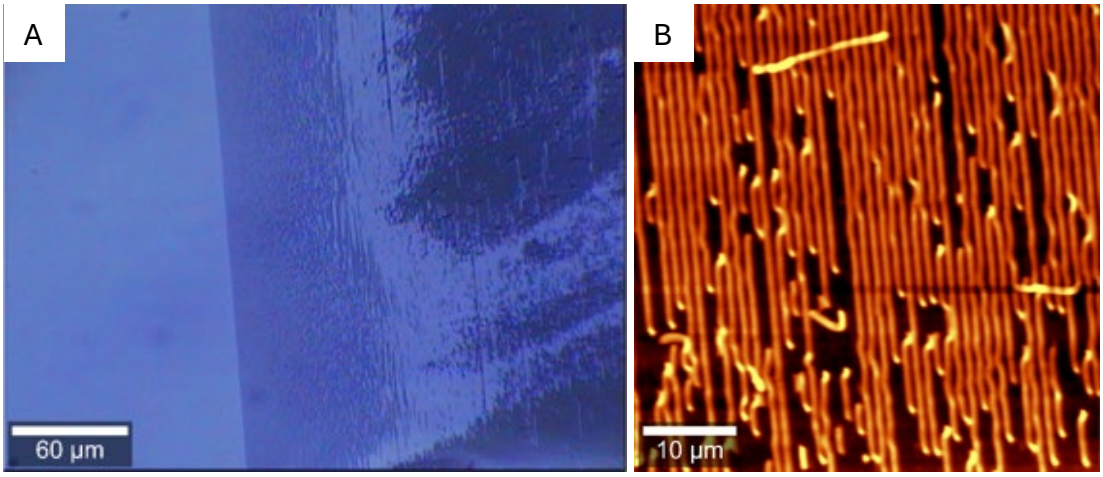

Figure 22: A) Optical image 20x of a PDMS stamp peeled the same day of his curing. B) AFM of the PDMS stamp with irregularities.

Conversely, peeling them the following day produced very uniform stamps. An image of a homogeneous stamp is shown at Figure 23 A), its AFM illustration and his height where it can be observed quite homogeneous is presented at Figure 23 B) and C).

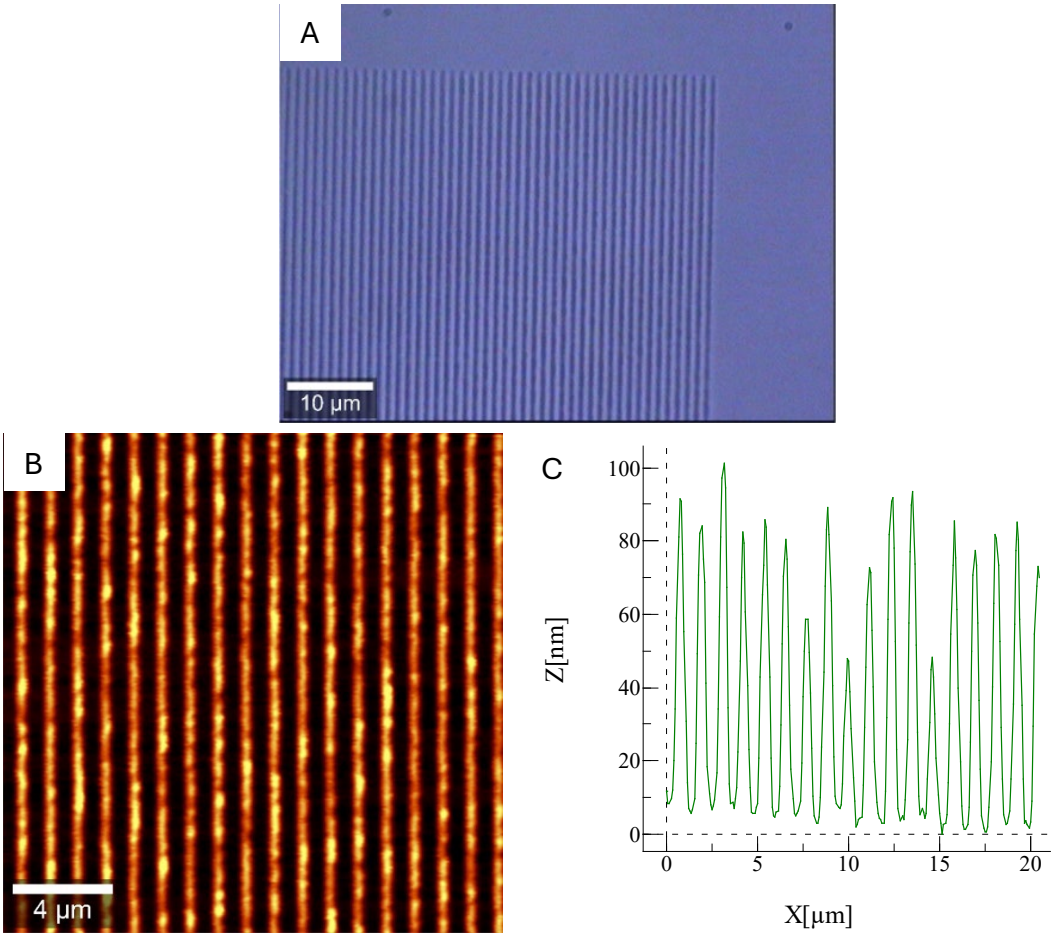

Figure 23: A) Optical image 100x of a homogeneous PDMS stamp. B) AFM image of the homogeneous PDMS stamp. Size: 20 um x 20 um. C) AMF profile of the PDMS stamp.

d) Another crucial aspect of the **peeling** process is the **direction** in which it is performed. It is important to peel in the same direction as the master's grating. Peeling perpendicular to the grating may cause the high parts of the PDMS pattern to break.

e) One more consideration was the importance of **cleaning the master after peeling the PDMS**, previous to its reuse for another stamping series. This precaution is advisable to remove any residual PDMS from the previous stamp, although usually it is not necessary to achieve optimal PDMS stamp quality. OM was employed to check if cleaning was required. In Figure 24 there is an image of the master with residual PDMS stuck. The cleaning process involved using sulfuric acid (H_2SO_4) at 80-90°C to remove the residual PDMS adhered to the master, followed by plasma cleaning.

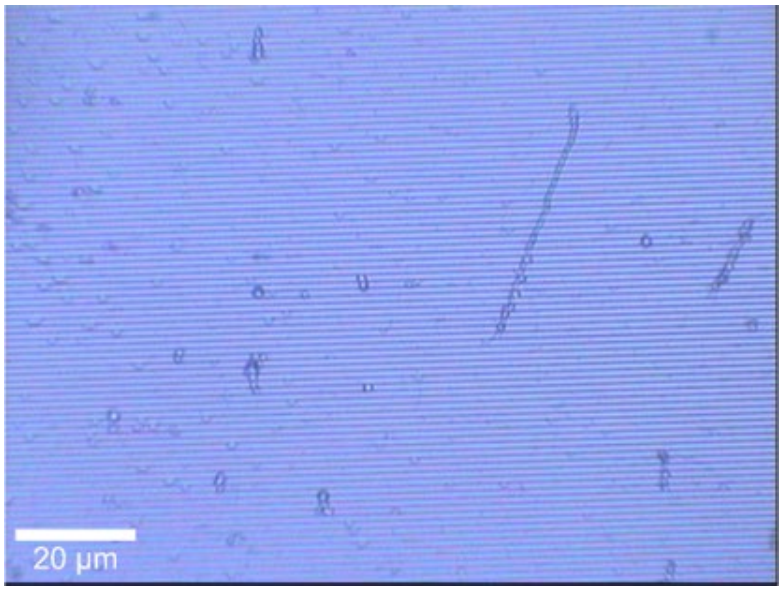

Figure 24: Optical image 50x of the master with residual PDMS.

f) Finally, the last aspect considered in the fabrication process of PDMS stamps was the **presence of an aluminium layer** on the master. Although it is generally preferable to peel the PDMS with an aluminium layer present on the master, it was investigated whether this layer was necessary given that this geometric pattern of the master had never been peeled before. As the layer was removed after each cleaning process, it was tried to peel without the aluminium layer, but the PDMS was stayed more stuck than if the master had aluminium.

4.1.3. Metasurface fabrication requirements and characterization

Once all the tests to determine the optimal characteristics of the PDMS stamps were completed, the focus changed to achieving the best metasurface samples. This required the use of multiple PDMS stamps and a significant number of Au substrates. It was studied the influence of the next parameters to optimize the metasurface fabrication.

a) Initially, there were difficulties with the solvent used to mix with the PMMA. Ethanol was used at first, but the PMMA did not dissolve well. Therefore, **ethanol was replaced with acetone**, and with slight stirring, the PMMA dissolved perfectly.

b) The next parameter optimized over several days was the **amount of PMMA solution** used in the process. Initially, the entire gold surface was covered with the PMMA solution, resulting in an excess of PMMA remaining on the surface. Subsequently, the samples were prepared using a single drop, which proved to be better. Finally, the optimal specification was to use the minimum possible amount of PMMA. The smallest amount of solution that could be deposited on the sample was 10 µl, due to the capillarity of the solution causing the drop to rise up the tip of the micropipette with less amount.

c) The following parameter optimized was **the transfer force** applied to transfer the PDMS pattern to the sample, to achieve the highest quality and most uniform samples. Initially, samples were compared with and without applied pressure. Excessive pressure deformed the bars of the PDMS grating stamp. So, using a dynamometer, a pressure of 0.2 N was applied, in Figure 25 there is an illustration of the dynamometer setup.

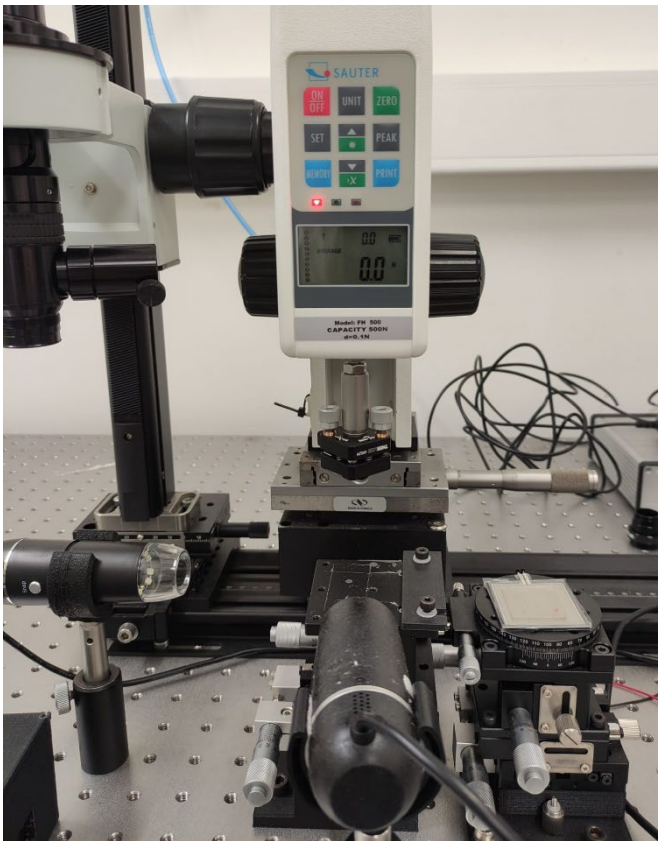

Figure 25: Dynamometer setup illustration

While the height achieved with both methods was similar, the stability was worse with the dynamometer than without pressure and the bars of the grating were deformed a little bit. There is an example of a sample made with the dynamometer where it can see the bars deformed with the OM in Figure 26 A), with the AFM in Figure 26 B) and with the height graphic of the AFM in Figure 26 C). To apply pressure more stably, a 55 g weight was used with a microscope slide and a weight over it, resulting in the highest quality gratings. The average heights of all gratings produced with different pressures are shown in Table 1.

Table 1: Average height transfer to the PMMA grating for different transfer forces.

Force (N)	Height transfer (nm)
0	40-60
0.2	60
0.54	90

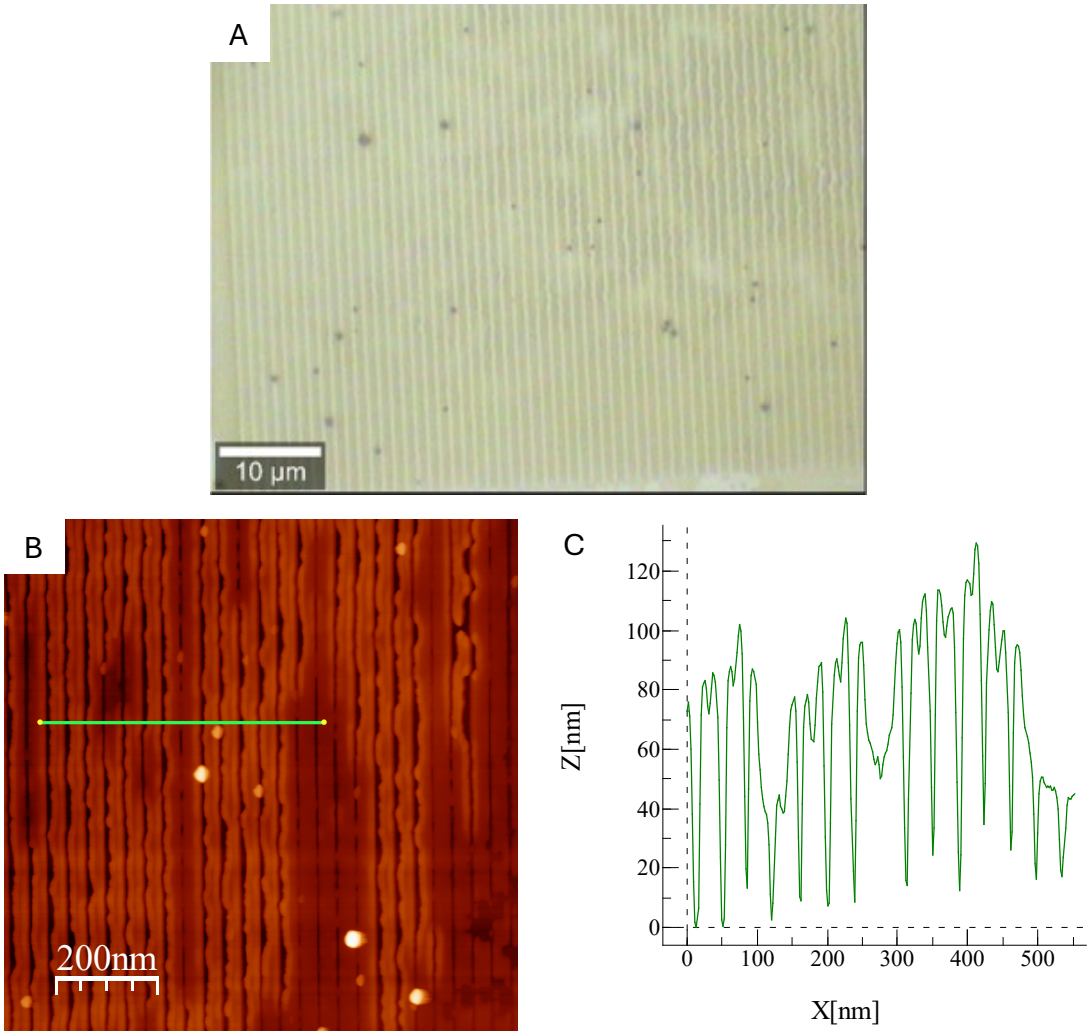

Figure 26: A) Optical image 100x of a metasurface made with dynamometer. B) AFM image of the deformed metasurface. Size: 1 um x 1um C) AFM sample profile.

d) The final aspect evaluated in the transfer of the PDMS pattern to the sample was the order of which one must be on the **bottom or on top**, the substrate or the PDMS stamp. Different configurations were tested, the conventional method with the substrate on the bottom and the PDMS stamp on top like Figure 27 A). It gives homogeneous metasurfaces how it is watched in the OM at Figure 27 B) and in the AFM at Figure 27 C). Also, with this method the size reached a height between 80 - 90 nm like is shown at Figure 27 D).

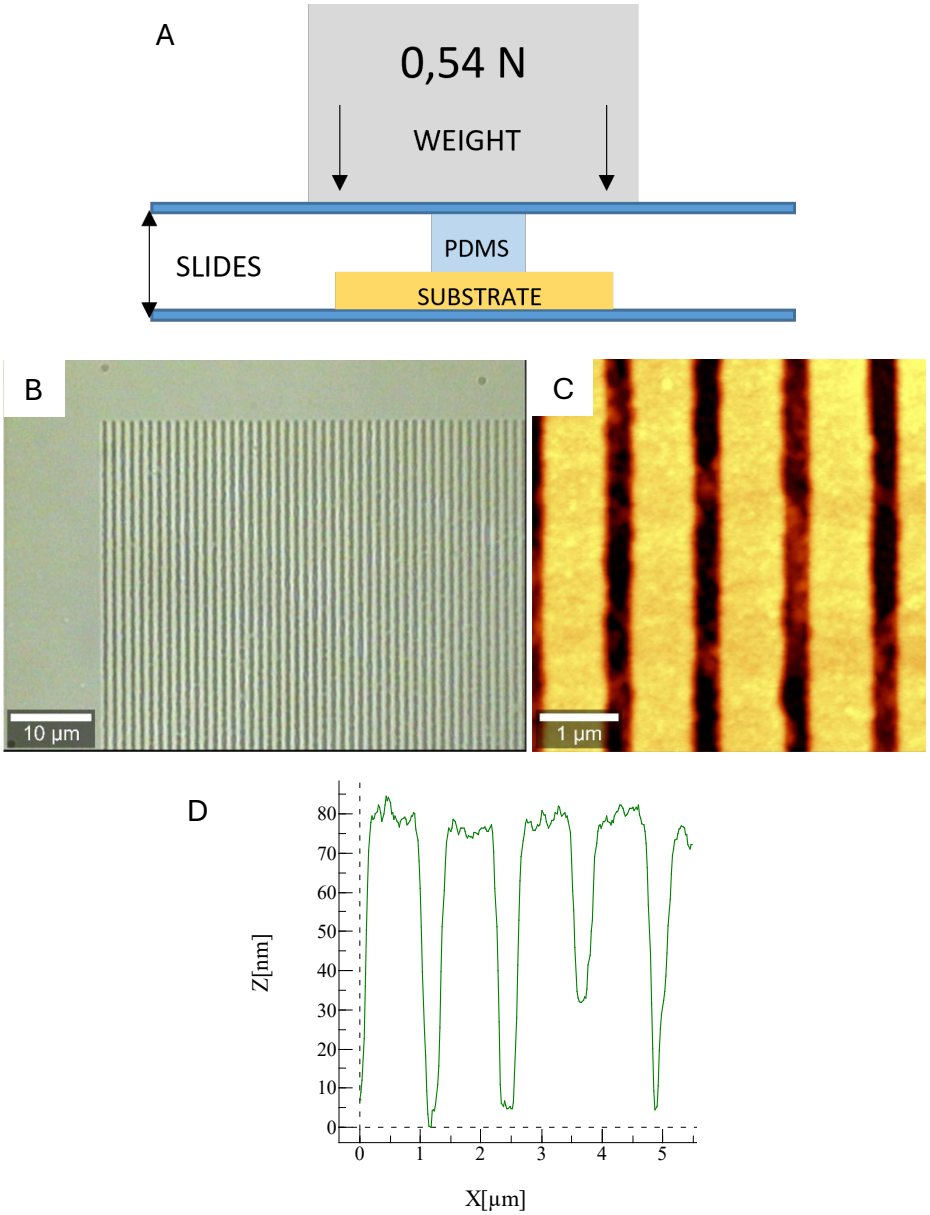

Figure 27: A) Conventional method with weight. B) Optical image 100x of a sample done with conventional method with weight. C) AFM image of a sample done with conventional method with weight. Size. 5 um x 5 um D) AFM sample profile.

The same configuration was proved without the application of weight like Figure 28 A). Although it can made homogeneous metasurfaces as it can be seen in Figure 28 B) with the AFM, the height of the samples is between 30 – 40 nm, lower than the previous configuration, in Figure 28 C) is shown the height of this method.

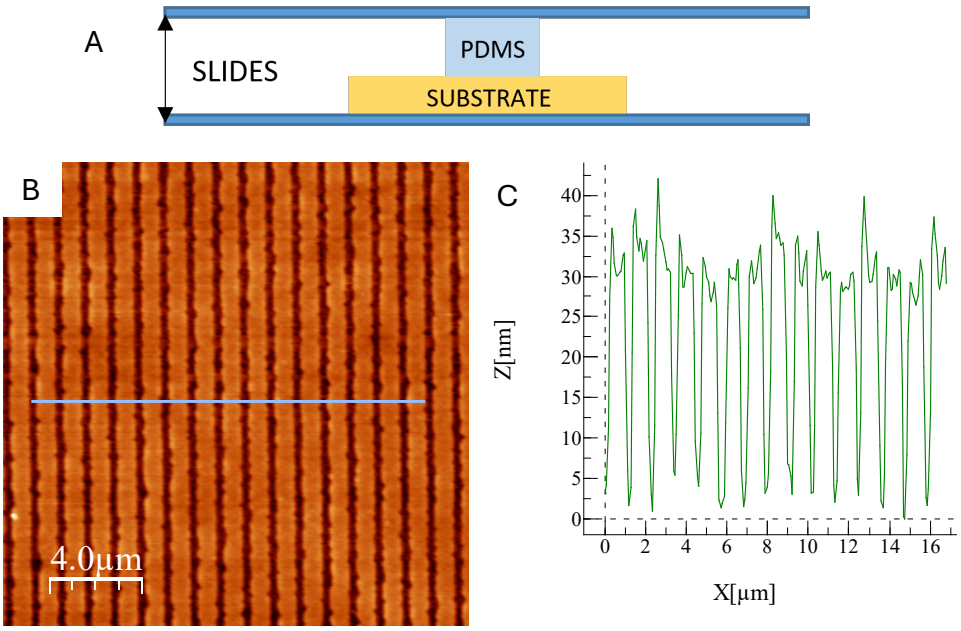

Figure 28: A) Conventional method without weight. B) AFM topography image of a sample done with conventional method without weight. Size: 20 um x 20 um C) AFM profile.

The inverted configuration with the PDMS stamp on the bottom and the substrate on top (upside-down method) like Figure 29 A), was the other way to achieve metasurface with a height between 80 – 90 nm like the graphic of the Figure 29 D). Even though the bars arrive to 100 nm, the gaps don't arrive to 0 nm. Despite of the optical image and the AFM shown at Figure 29 B) and C) seems to be homogeneous, it had not the same uniformity in all the sample.

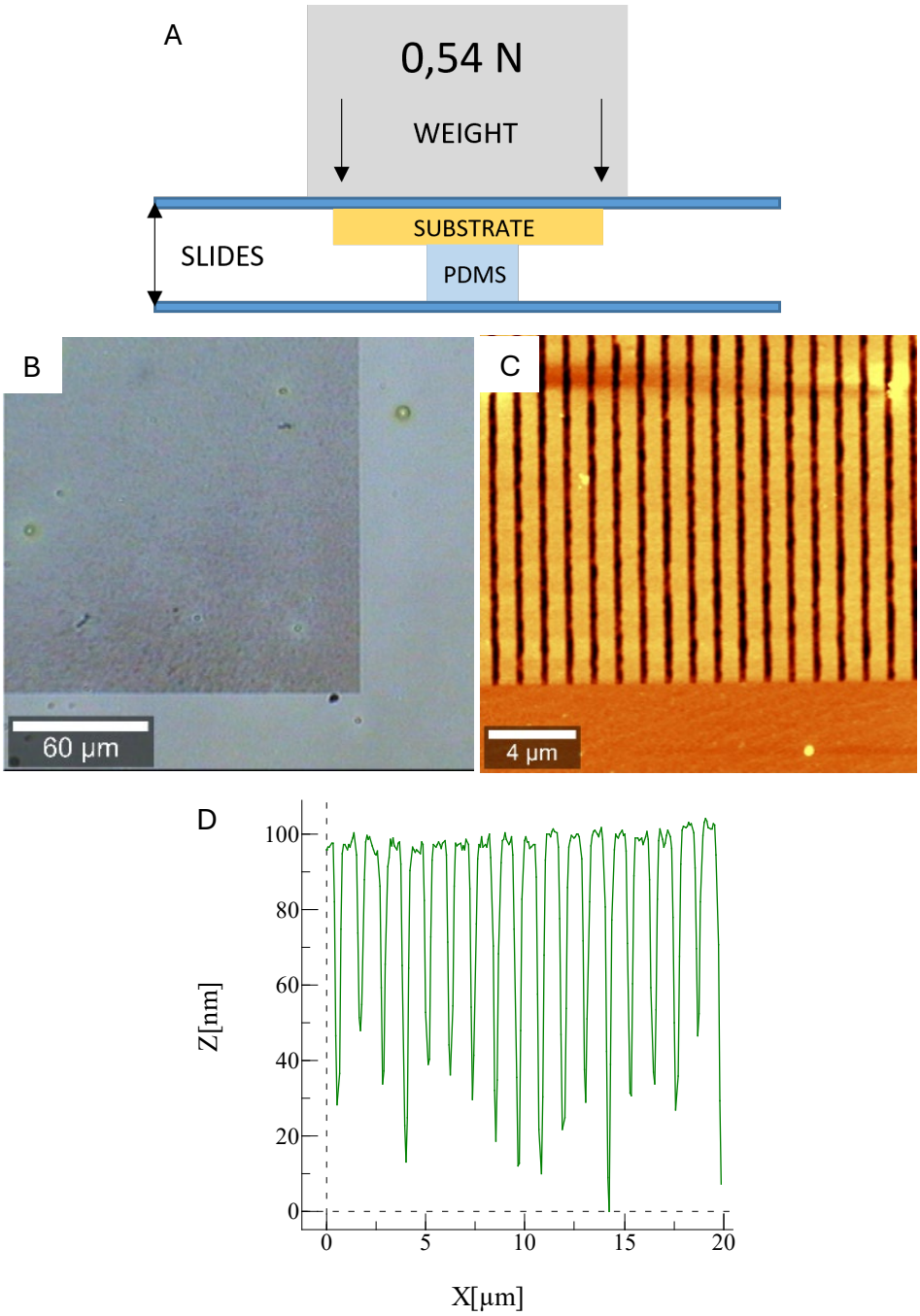

Figure 29: A) Upside-down method with weight. B) Optical image 20x of a sample done with upside-down method with weight. C) AFM topography image of a sample done with upside-down method with weight. Size 20 um x 20 um. D) AFM profile.

The last configuration proved was the upside-down method without weight like Figure 30 A). Just like with the weight, despite the AFM looks good in some areas at Figure 30 B), the sample is not homogeneous in all the metasurface. The height of this method was around 50 nm because in Figure 30 C) there is some gaps which don't arrive to 0nm.

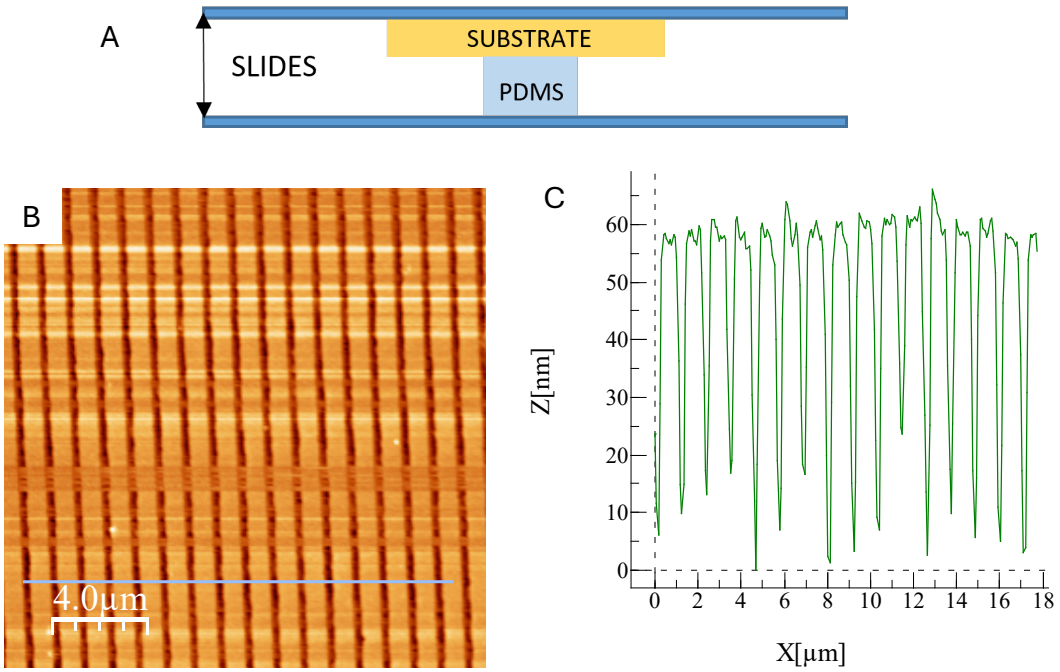

Figure 30: A) Upside-down method without weight. B) AFM of a sample done with upside-down method without weight. Size 20 um x 20 um D) AFM profile.

The maximum height of 90 nm was achieved in both methods when weight was applied. **However, the conventional method proved to be** more comfortable for his stability and reach **more homogeneous metasurfaces**. So, the optimal configuration of the pattern transfer is the same as Figure 27 A), with the following process. Initially, the substate is positioned onto a microscope slide, followed by the drop of the PMMA solution. After, the PDMS stamp, with another microscope slide stuck on it for improved manipulation, is rapidly placed over the sample. After approximately 7 minutes, the PDMS stamp can be delicately withdrawn, leaving the sample with the master pattern intact.

Unfortunately, sometimes the PDMS stamp peeled off the gold surface, leaving the stamp unusable due to the gold adhering to it. This issue appeared because some of the substrates had manufacturing defects. In certain cases, the gold surface was partially peeled even before the transfer process. In Figure 31 there is an example of one of the PDMS stamps which was unusable after trying to transfer the pattern to a gold substrate.

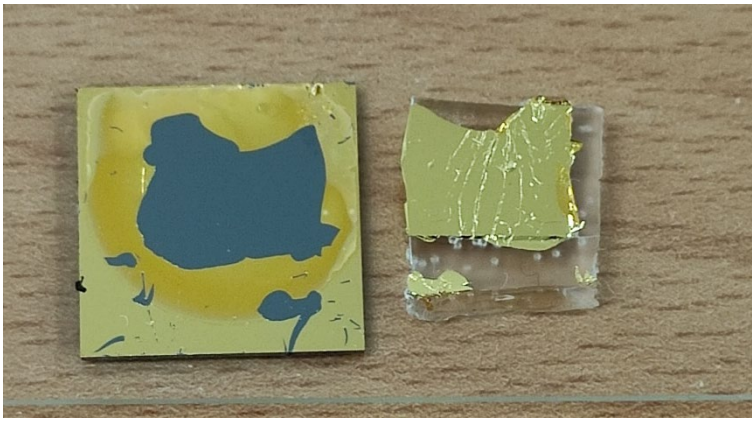

Figure 31: Substrate peeled and a PDMS stamp with gold stuck after a failed pattern transfer.

4.1.4. Metasurface fabrication with SCO NPs requirements and characterization

Once the optimal pattern transfer process was established to fabricate the PMMA gratings, the next step was to create the hybrid metasurfaces with the PMMA/SCO NPs. Initially, it was tried to filter the solution, without PMMA, to remove potential agglomerates that could appear in the samples. The solution was filtered using a syringe filter with a pore size of 0.22 µm. However, agglomerations still appeared after filtration as it can see in Figure 32. So, the syringe filter was not used for other samples; instead, the solution was simply shaken with a magnetic stirrer. The different samples seemed to have a similar number of agglomerations.

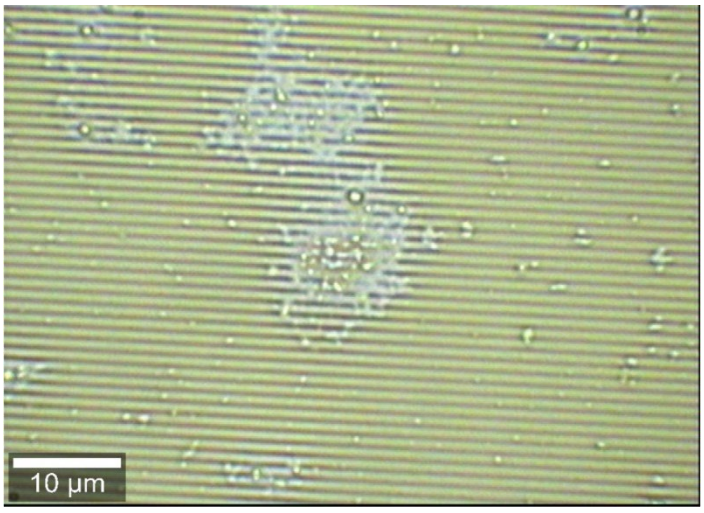

Figure 32: Optical image 100x of a metasurface with SCO NPs agglomerations.

Then to check the height and the quality of the sample with SCO NPs, it was measured a sample with the AFM in an area without too many agglomerations which is shown in Figure 33 A) and B). The height of the metasurface was around 50 nm like

Figure 33 C) where there is the height of the NPs over the sample. This could be due to the SCO NPs agglomerations, which interfere with the pattern transfer.

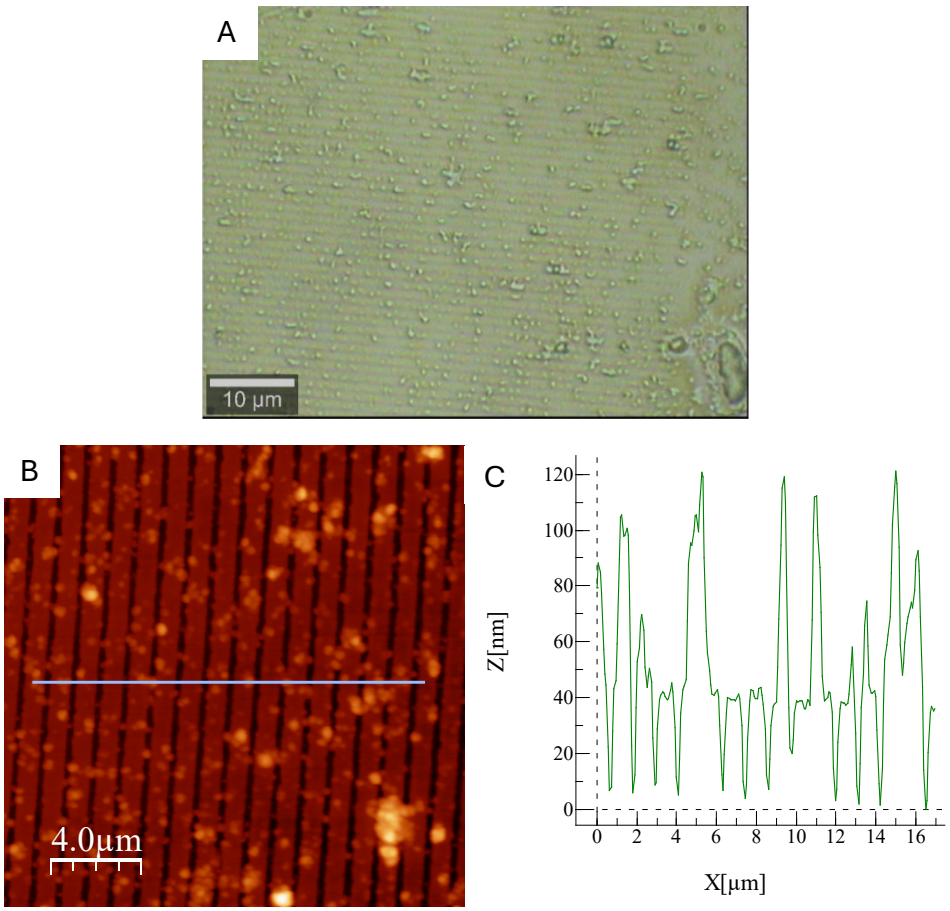

Figure 33: A) Optical image 100x of a metasurface with SCO NPs. B) AFM topography image of the hybrid metasurface with SCO NPs. Size 20 um x 20 um. C) AFM profile.

4.1.5. Characterization of the SCO NPs

It was measured a sample in a silicon surface with the Raman spectrometer, given that in an Au surface the surface plasmon exited by the 532 nm Raman laser can hide the SCO characteristic peaks. In Figure 34 A) there is the metasurface with SCO NPs, performed on silicon surface measured with the Raman which was performed at 532 nm (green) excitation, P = 1,1mW power, grating 600 l/mm and objective 50x. The single spectrum was scanned with 4 accumulations and with 30 s integration time per each accumulation. The Figure 34 B) shows the different peaks of the sample. The peak 1044 cm^{-1} is from the NO_3 and the peaks 1367 cm^{-1}, 1479 cm^{-1} and 1548 cm^{-1} are from the triazole. The highest peaks (more intense) are from the silicon, they are the 304 cm^{-1} which correspond with the TA mode of Si, the 521 cm^{-1} which correspond with the crystalline Si and around the 970 cm^{-1} which correspond with SiO_2. The peaks of the low spin (LS) and high spin (HS) mode of the SCO NPs are between 90 cm^{-1} and 200 cm^{-1}. The peak 95 cm^{-1} of the Figure 34 B) is from the LS because the sample is in ambient

temperature, for now the HS couldn't be seen because there is not a setup with a Raman spectrometer and a heating plate.

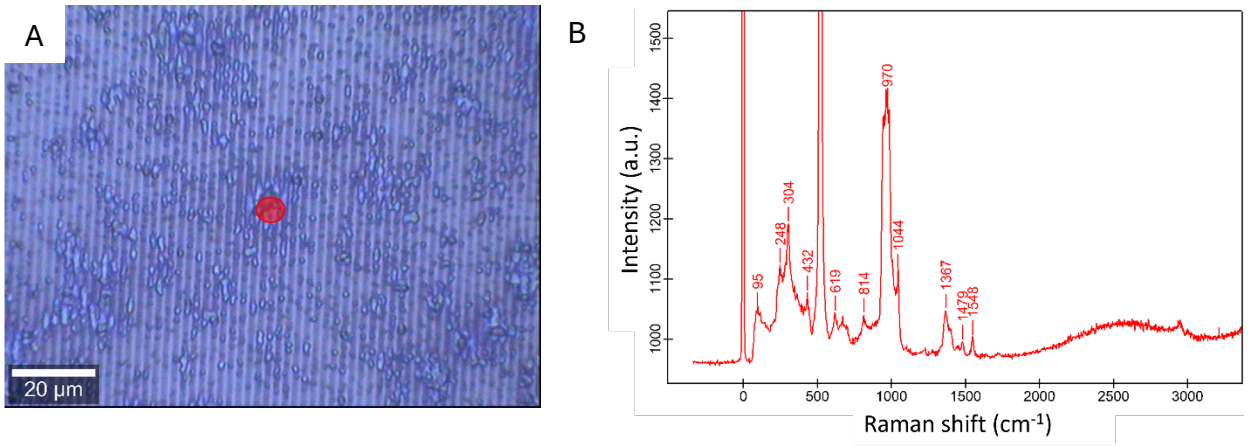

Figure 34: A) Optical image 20x of a metasurface with SCO NPs on silicon surface. B) Raman single spectrum of the SCO NPs with silicon.

Moreover, the SCO NPs where analyse with the SEM using SEM to examine their distribution on the metasurface. In Figure 35 A) shows an SEM image of a metasurface with SCO NPs. Figure 35 B) presents the spectrum of the metasurface without NPs, while the spectrum of the metasurface with SCO NPs is in Figure 35 C).

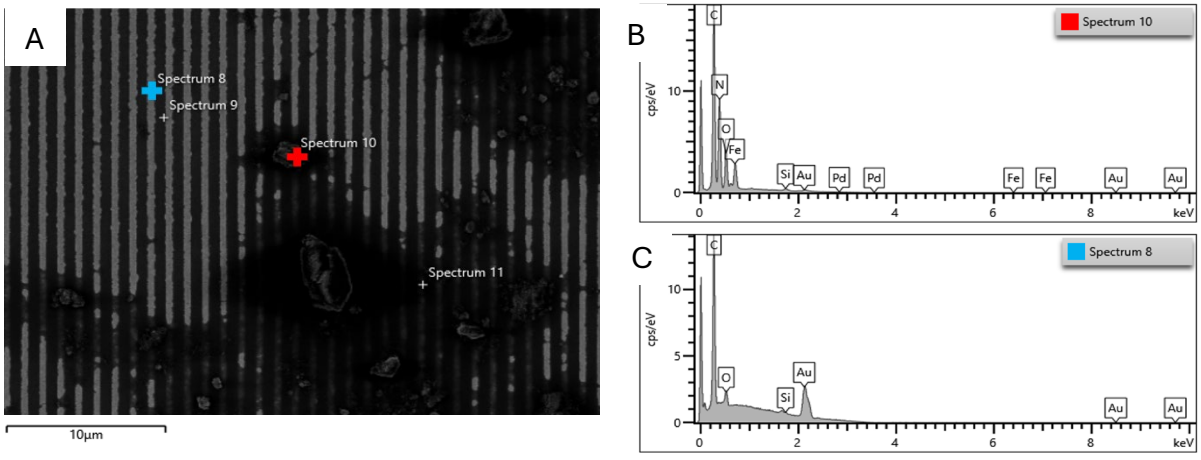

Figure 35: A) SEM of the metasurface with and without SCO NPs. B) EDX spectrums of two different areas in the grating sample: Red spectrum corresponds to an area with the SCO NPs and blue spectrum corresponds to an area of metasurface without SCO NPs.

As shown in the spectrum of Figure 35 B), the measurement on the SCO NPs contains peaks for Fe and N, indicating the presence of SCO NPs. In contrast, the spectrum of Figure 35 C) taken outside the NPs shows only peaks for C and O, which are components of the PMMA polymer, and Au from the substrate. We could infer that despite the use of a magnetic shaker and filtering, it was not possible to avoid NP agglomeration.

4.2. Conclusion and Future Work

To summarize, a large number of experiments were performed to optimize the PDMS stamps and the fabrication of the metasurface. First, the dimensions of the master were set and characterized, resulting in a grating of 1 mm x 1 mm. Then it was characterized with AFM, which revealed that the AFM tip could not measure the full depth of the master due to the narrow bars of the grating. After the master was made, it was optimized the parameters of the PDMS stamp and his fabrication like the thickness, the time of curing, the time for peeling, the direction of the peeling, if the master was cleaned and the aluminium layer of the master. Furthermore, it was established the features of the metasurface fabrication through repeating several times the pattern transfer. The parameters studied were the chemical used it for mixing the PMMA, the amount of solution dropped, the application of pressure with and without the dynamometer, the use or not of a weight and the configuration of the pattern transfer mode. The majority of this prove were checked with the AFM and the optical microscope characterization which were the instrument most used in this project. Finally, it was done the metasurface with the SCO NPs and they were characterized with the Raman spectrometer and the SEM to see the principal components of the NPs.

The objective of manufacturing metasurface by soft lithography was accomplished successfully. Combining all the optimized features of the PDMS stamp fabrication and metasurface fabrication processes, it was achieved uniform samples with a height of 90 nm. The enhanced transfer method reached optimized the maximum height of the PDMS stamps which was 90 nm too. Unfortunately, the height of the metasurface design of 500 nm, which is set in Figure 20 A), was not reached to mimic the PDMS stamp topography. Probably, it is because the structure of the master is very narrow and the PDMS can't flow through the grating. A future work thought for trying to fix this problem is waiting some hours after the PDMS is deposited onto the master and before it is cured in the oven. The reason of this is to let the PDMS flows between the grating bars.

Other future work planned is to make the metasurface with photolithography. The idea will be making spin coating with the solution of PMMA with SCO NPs and making the pattern with photolithography on the PMMA layer. In this way it is possible to reach the specifications of the metasurface geometry. Although, this method is more expensive than soft lithography.

CHAPTER 5. POSITIONING OF INDIVIDUAL $BATIO_3$ NANOPARTICLES BY INKJET PRINTING.

5.1. Results and Discussion

5.1.1 Optimization cleaning substrates process

Several methods were tested for cleaning the SiO_2 substrates. First, tests were done with water. The initial method, described in the materials and methodology section, involved using acetone and IPA. This cleaning process made the substrate more hydrophilic, as Figure 36 B), shows compared to an untreated substrate like Figure 36 A), yet the droplets maintained a good shape, though slightly larger.

The second cleaning method applied was oxygen plasma treatment. This method made the substrate highly hydrophilic, preventing droplet formation as it can be seen in Figure 36 C). In these experiments, the droplet volume was 2500 pl, and the distance between droplet centres was 400 µm.

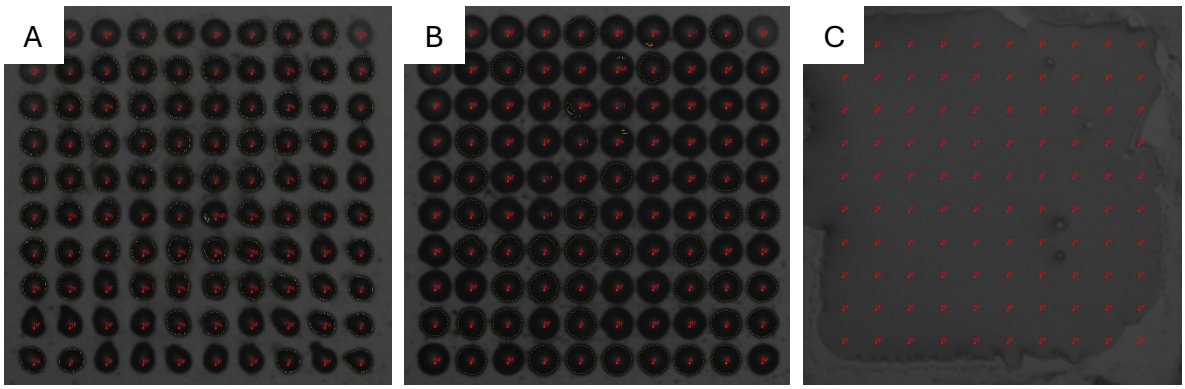

Figure 36: A) Substrate without cleaning. B) Substrate cleaned with acetone and IPA. C) Substrate cleaned with oxygen plasma.

Subsequently, a smaller volume of 1500 pl was tested to prevent the droplets from being too close to each other. FIGURE 1A shows the droplets at this reduced volume. Once the inkjet printer parameters were established, a sample with $BaTiO_3$ NPs was prepared. Visually, it appeared identical to Figure 37 A), so it was analysed using an OM. Figure 37 B) show the sample with $BaTiO_3$.

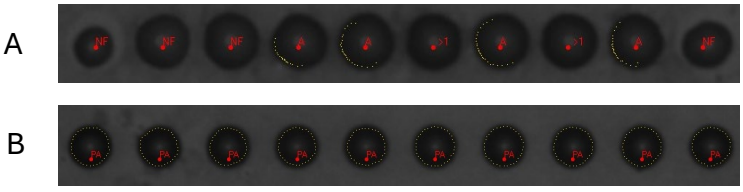

Figure 37: A) Substrate with only ultrapure water. B) Substrate with $BaTiO_3$ NPs

5.1.2. Characterization of the $BaTiO_3$ NPs

Once the NPs were deposited, they were characterized with the OM. Only 7 NP agglomerations were observed at the expected droplet locations. In the remaining 3 locations, it appears that no NPs were deposited with the droplets. Raman measurements were made at the spots where NPs were present to confirm they were $BaTiO_3$. Figure 38 A), B) and C) shows an NP agglomeration with different optical microscope magnifications 10x, 50x and 100x respectively.

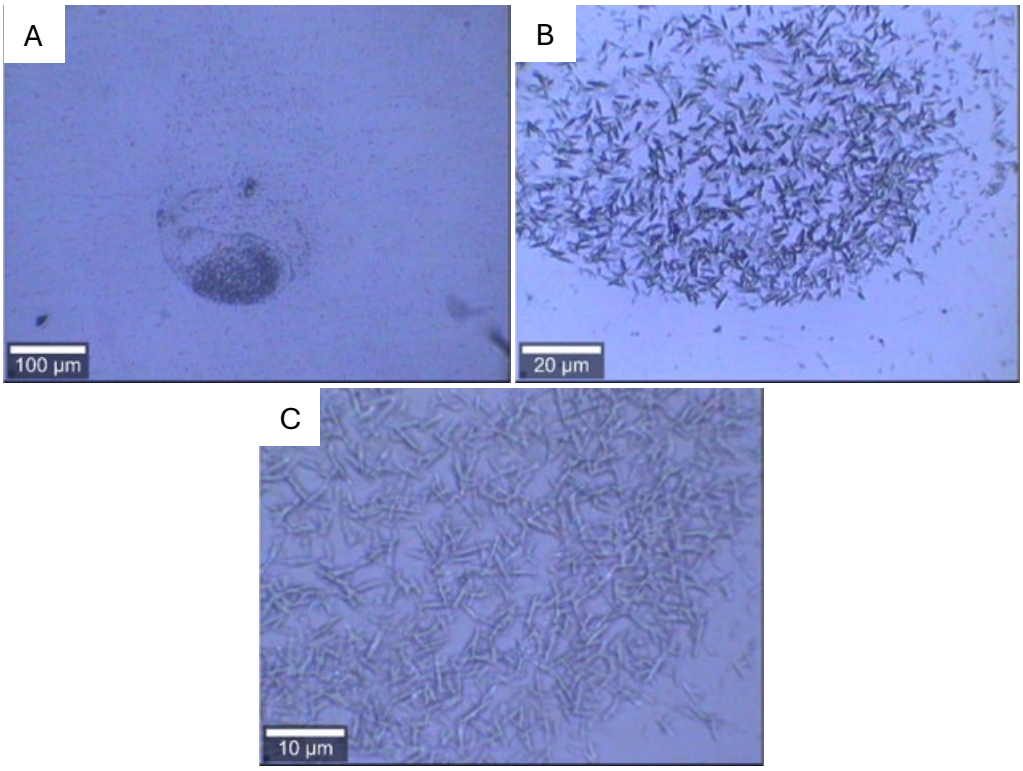

Figure 38: A) Optical image 10x of an NPs agglomeration. B) Optical image 50x of an NPs agglomeration. C) Optical image 100x of an NPs agglomeration.

Then, it was made a Raman spectroscopy on the agglomerations of NPs to confirm it was $BaTiO_3$. In Figure 39 B) there is the spectrum where we can see the principal peaks are similar to the measurements made by Dr. Javier Hernandez-Rueda, our collaborator from Universidad Complutense de Madrid, which are in Figure 39 A). The Raman measurements were performed at 532 nm (green) excitation, P = 27,8 mW power, grating G = 600 l/mm and objective 100x. The number of accumulations were 10 with 10 s of integration time at each accumulation.

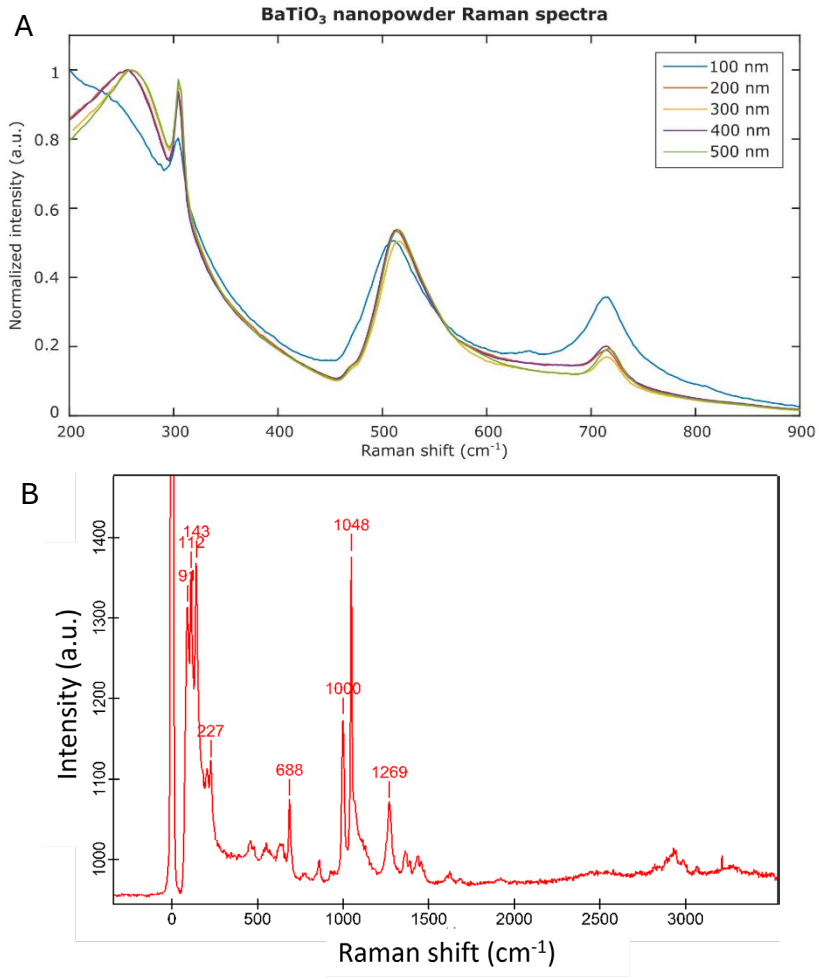

Figure 39: A) $BaTiO_3$ NPs Raman spectra by Dr. Hernendez-Rueda. B) Raman spectrum of $BaTiO_3$ NPs on glass substrate.

Furthermore, it was made a Raman spectroscopy of the substrate to compare the noise induced by the glass in the $BaTiO_3$ spectrum. In Figure 40 it can be seen that the peaks from 111 cm^{-1} to 1098 cm^{-1}, correspond to the resonances of the glass substrate.

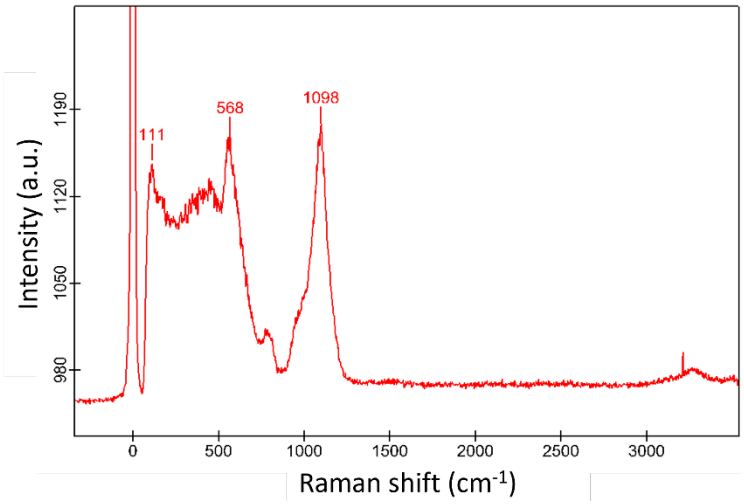

Figure 40: Raman spectrum of the glass substrate.

5.1.3. Experiments with the lithographed marks

Since it was challenging to locate the NPs after their deposition, a matrix of 10 per 10 marks was lithographed to facilitate the analysis of NPs within the marks. The design consisted of a ring with an internal diameter of 200 µm and a separation of 500 µm between individual marks. Figure 41 shows the design of the marks and the matrix distribution.

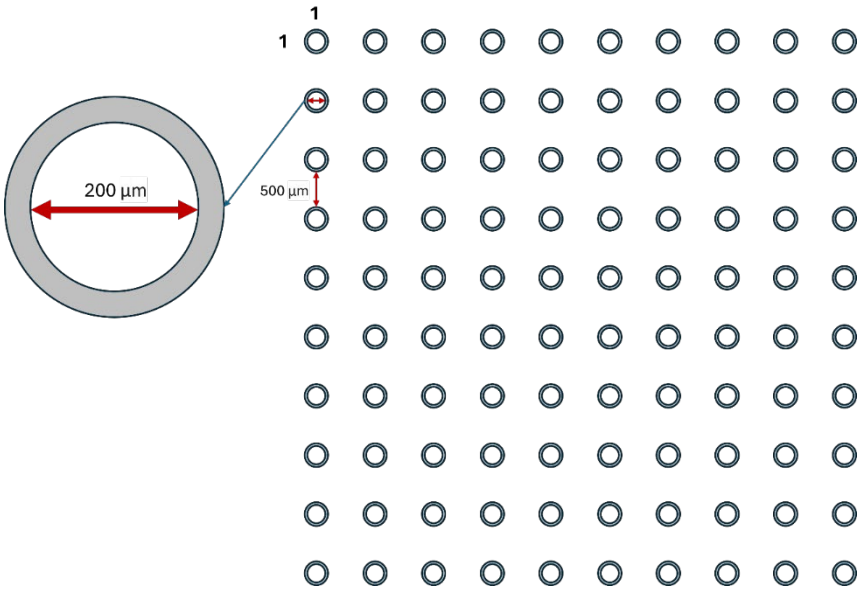

Figure 41: Marks and matrix dimensions.

After the fabrication team make the marks on a substrate (fabrication performed at NTC facilities), it was tried to deposit some droplets by inject printing. However, the treatment used to lithograph the marks made the substrate very hydrophilic, making it difficult to deposit the drops within the marks. In Figure 42 A) the

contact angle of the sample after the lithography is shown. To resolve this problem, different treatments to make the substrate more hydrophobic were tested. The first one was cleaning the substrate with water vapor plasma, nevertheless it didn't make the substrate hydrophobic, as expected. The contact angle shown in Figure 42 B) was similar to the sample without any treatment. Then, hydrogen plasma was tested, but the hydrophobicity was as low as the first one like it is shown in Figure 42 C). Finally, an annealing treatment was proved in an oven at 200 ºC in argon atmosphere of 2 l/min for 30 minutes. The sample became significantly more hydrophobic as is shown in Figure 42 D).

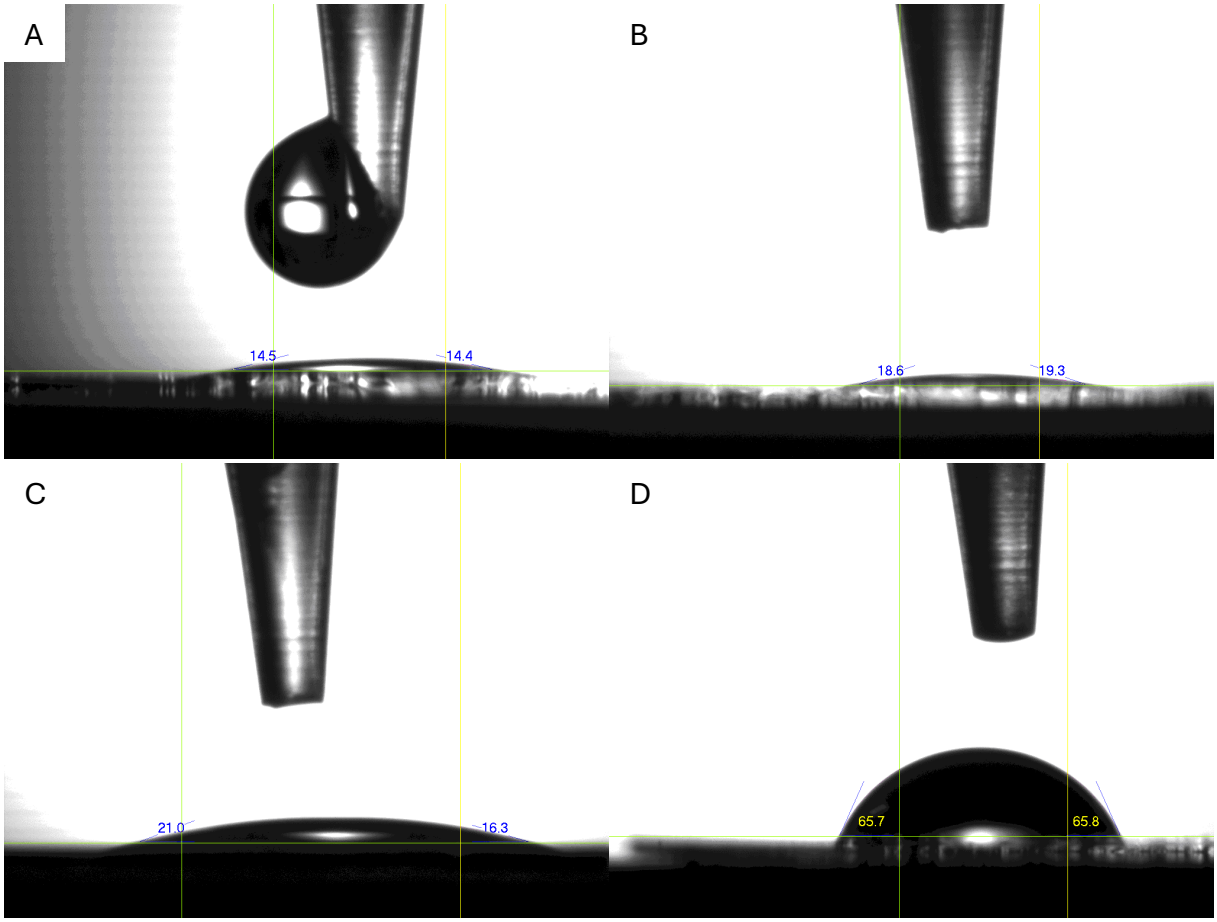

Figure 42: A) Contact angle test of the substrate with marks. B) Contact angle test of the substrate with marks treated with water vapor plasma . C) Contact angle test of the substrate with marks treated with hydrogen plasma. D) Contact angle test of the substrate with marks treated with annealing.

Subsequently, to the dropping of NPs within the marks was carried out using a concentration of 2 mg of $BaTiO_3$ NPs per 20 ml of ultrapure water. Unfortunately, the checking with the OM didn't show any NPs in the sample. It could be due to the tip of the inkjet printer didn't take any NPs from the well.

These last attempts trying to deposit NPs with the substrate hydrophilic and hydrophobic show how challenging is to place NPs with the inkjet printer.

5.2. Conclusion and Future Work

To summarize, lots of attempts were made to deposit $BaTiO_3$ NPs with the inkjet printer. Initially, various methods were tested trying to clean the substrate as clean as it was possible without affecting the droplet deposition. It was concluded that the best way was cleaning them with acetone and IPA. Then, some $BaTiO_3$ NPs were successfully deposited in the first attempts on the sample without marks. However, this made it difficult to localize the NPs using OM.

When the NPs were confirmed to be deposited on the glass substrate, they were characterized with Raman spectrometer. Then, next step involved the fabrication of lithograph marks in the substrates to localize the NPs easier, and to separate the NPs with the distance required and to differentiate easier between different $BaTiO_3$ NPs size or different concentrations of the same size $BaTiO_3$ NPs.

After lithography of the glass substrate, the sample was too hydrophilic to deposit de drops correctly. So, it was treated with various cleaning methods like acetone and IPA, different types of plasma treatments and finally with an annealing in an argon atmosphere. This last method was the one which increased the hydrophobicity of the sample. Anyway, when droplets containing NPs were deposited, no NPs could be observed inside the marks using the OM.

The goal of deposit $BaTiO_3$ NPs with precision was achieved, but when it was tried to deposit them in the marks was unsuccessful. Future work to solve this problem could be using a higher concentration of NPs, despite the risk of clogging the printer tip.

This project requires further work to facilitate the deposition of NPs and to make more experiments with the different available sizes of $BaTiO_3$ NPs to achieve project's objectives.

CHAPTER 6. CONCLUSIONS AND FUTURE WORKS

To summarize the work done in this thesis**, the principal objective of developing nanolithography methods and achieving controlled deposition of NPs was accomplished** with varying degrees of success across different projects. Overall, positive progress was made in all three projects.

In the case of the optomechanical cavities, it was determined that using a powerful red laser to move Au NPs can potentially damage the sample guide and burn the structure. Despite this, **the experiments demonstrated that it is possible to move NPs with a laser, paving the way for future research**. Future work includes experimenting with lasers of different wavelengths, using lower power and energy to move the NPs, and exploring other methods to position NPs in the center of the optomechanical cavities to achieve optimal sensing signals.

For the fabrication of reconfigurable metasurfaces, **the principal goal of replicating a homogeneous pattern from the master via soft lithography was successfully achieved so the hybrid metasurface was fabricated**. Ongoing efforts are focused on achieving an optimized stamp geometry and the use of photolithography to create higher patterns.

In the final project, **$BaTiO_3$ NPs were successfully deposited, and the location of NP placement was optimized by lithographing marks on the substrate**. Although this task proved challenging, with NPs being deposited successfully in the first attempts, the groundwork has been laid for future improvements. Future work includes experimenting with higher concentrations of smaller NPs to prevent tip blockages, which should enhance the consistency and reliability of $BaTiO_3$ NP deposition onto the glass substrates.

CHAPTER 7. SUSTAINABLE DEVELOPMENT GOALS

Degree of alignment of the work with the Sustainable Development Goals (SDGs).

Table 2: Sustainable Development Goals

Sustainable Development Goals	High	Medium	Low	Not applicable
SDG 1. **No poverty.**				X
SDG 2. **Zero hunger.**				X
SDG 3. **Good health and wellbeing.**				X
SDG 4. **Quality education.**				X
SDG 5. **Gender equality.**				X
SDG 6. **Clean water and sanitation.**				X
SDG 7. **Affordable and clean energy.**	X			
SDG 8. **Decent work and economic growth.**				X
SDG 9. **Industry, innovation and infrastructure.**	X			
SDG 10. **Reduce inequalities.**				X
SDG 11. **Sustainable cities and communities.**				X
SDG 12. **Responsible consumption and production.**				X
SDG 13. **Climate action.**				X
SDG 14. **Life below water.**				X
SDG 15. **Life on land.**				X
SDG 16. **Peace, justice and strong institutions.**				X
SDG 17. **Partnerships for the goals.**				X

This work is framed within the development of low consumption and not polluting technologies, so we can englobe it within two Sustainable Development Goals: SDG 7 and 9. The use of nanomaterials (such as the NPs discussed in this work) and their application in low consumption and low-cost photonic devices are expected to have high impact in the development of cleaner and more accessible technologies. Additionally, these devices contribute to the innovative fabric of our sector (integrated photonics), and it is expected that the industry incorporate these technologies in the short to medium term.

CHAPTER 8. BUDGET

8.1. Introduction

This part of the writing provides a list of the economic resources spend in all the research work, including the workers, the machinery and the materials used in each project.

The workers were a biomedical engineer student and two co-tutors of the projects. Also, there were some task were it was necessary the aid of a technical specialist. The Equation 2 is used to calculate the cost of a worker.

$$Worker\ cost = Gross\ salary + Social\ security\ cost \quad (2)$$

Equation 2

Applying specific percentages of the gross salary of the worker, the Social security cost is calculated. The contributions are 23.6% for common contingencies, 5.5% for unemployment for permanent contracts, 1% for accidents at work and occupational diseases for office workers, 0.6% for vocational training, and 0.2% for the Fondo de Garantía Salarial (FOGASA). The cost calculation is shown in Equation 3.

$$Social\ security\ cost = Gross\ salary * (0{,}236 + 0{,}055 + 0{,}01 + 0{,}006 + 0{,}02) \quad (3)$$

Equation 3

Considering the holiday period and annual bonus, the estimated annual salary for a tutor, who is a university professor, is approximately 3500 €, while the salary for an engineering student is 1100 €. The annual SSC for the professor tutor (PT) is shown in Equation 4 and for the biomedical engineering student (ST) is in Equation 5.

$$Annual\ SSC\ PT = 12978\ \frac{€}{year} \quad (4)$$

Equation 4

$$Annual\ SSC\ ST = 4078{,}8\ \frac{€}{year} \quad (5)$$

Equation 5

The annual cost for the tutor, Equation 6, and for the student, Equation 7, are:

$$Annual\ PT\ cost = 3500\ \frac{€}{month} * 12 + 12978 = \ 54978\ \frac{€}{year} \quad (6)$$

Equation 6

$$Annual\ ST\ cost = 1100\ \frac{€}{month} * 12 + 4078{,}8 = \ 17278{,}8\ \frac{€}{year} \quad (7)$$

Equation 7

The remaining days of working without the holidays and the free days in a year are 224 days. Working 8 hour each day, the cost per hour for the tutor and for the student are calculated in Equation 8 and Equation 9 respectively.

$$PT\ cost\ per\ h = \frac{54978\frac{€}{year}}{224\frac{days}{year}*8\frac{h}{day}} = 30{,}68\ \frac{€}{h} \quad (8)$$

Equation 8

$$ST\ cost\ per\ h = \frac{17278{,}8\frac{€}{year}}{224\frac{days}{year}*8\frac{h}{day}} = 9{,}64\ \frac{€}{h} \quad (9)$$

Equation 9

Being 30,68 €/h for the tutor and 9,64 €/h for the student.

The machinery amortization costs provided by the Nanophotonics Technology Center (NTC) is 45 €/h per equipment and for the clean room equipment is 90 €/h. Finally, the budget for the materials is obtained adding 15 % overheads and 6 % of industrial profit, and 21 % for IVA to calculate the total budget.

8.2. Detailed Budget

The detailed budget was obtained using the software CYPE ARQUIMEDES student version. It consists of the several tables below:

- Table 2. Labour cost table.
- Table 3. Machinery cost table.
- Table 4. Materials cost table.
- Table 5. Unit price cost table.
- Table 6. Partial budget.

- Table 7. Contractual implementation budget.

Table 3. Labour cost table

Labour Table

Num.	Code	Labour designation	Price	Hours	Total
1	L.01	Thesis tutor distinguished researcher	30,68	41,00h	1.257,88
2	L.02	Thesis tutor cathedratic in photonics	30,68	15,00h	460,20
3	L.TS	Technical specialist	15,66	15,00h	234,90
4	L.IBE	Biomedical engineer student	9,64	233,00h	2.246,12
			Total	labour cost:	4.199,10

Table 4. Machinery cost table

Machinery Table

Num.	Code	Machinery designation	Price	Quantity	Total
1	EQ.R	Coater EVG 101	90,00	3,00h	270,00
2	EQ.DFg	Dark field optical microscopy	90,00	4,00h	360,00
3	EQ.ET	Etching: RIE ICP	90,00	4,50h	405,00
4	EQ.LIT	Raith 150 (lithography)	90,00	2,00h	180,00
5	EQ.INK	Inkjet printer	90,00	15,00h	1.350,00
6	EQ.INKs	SciFLEX_S3	90,00	15,00h	1.350,00
7	EQ.THA	Thermal Annealing	90,00	1,00h	90,00
8	EQ.PVA	Tepla PVA	90,00	2,00h	180,00
9	EQ.GON	Goniometer Ramé-Hart	45,00	4,00h	180,00
10	EQ.US	Ultrasonic cleaner	45,00	1,50h	67,50
11	MAT.MICRO	Optical microscope	45,00	7,00h	315,00
12	EQ.RA	Spectrometer alpha300 (Raman-AFM) (WITEC)	45,00	74,00h	3.330,00
13	EQ.RAs	Software Project 4.0 (Witec)	45,00	74,00h	3.330,00
14	EQ.SCA	Software DROPImage Pro	45,00	4,00h	180,00
15	EQ.SEM	Scanning electron microscope (SEM)	45,000	4,00h	180,00
16	EQ.LW11	Windows 11	0,001	50,00h	0,05
17	EQ.LO365	Office 365	0,001	50,00h	0,05
18	EQ.LO	Libre Office License	0,001	40,00h	0,04
			Total	machinery cost:	11.767,64

Table 5. Materials cost table

Materials Table

Num.	Code	Material designation	Price	Quantity	Total
1	MAT.mPIP2	Micropipette 10-100 µL	310,51	1,000u	310,51
2	MAT.mPIP	Micropipette 0,5 - 10 µL	310,51	2,000u	621,02
3	MAT.PMMA	PMMA (Polymethyl methacrylate)	227,00	1,000u	227,00

4	MAT.NP150	150 nm diameter gold spherical nanoparticles	195,00	1,000L	195,00
5	MAT.PDMS	PDMS	170,00	1,100kg	187,00
6	MAT.AFM	AFM probe	50,00	3,000u	150,00
7	MAT.IPA	Isopropanol	49,00	0,100L	4,90
8	MAT.APTES	APTES (3-Aminopropyl) triethoxysilane	44,50	1,000u	44,50
9	MAT.CLS	Clean room suit	38,00	4,000u	152,00
10	MAT.AC	Acetone	36,10	0,600L	21,66
11	MAT.ET	Ethanol	28,80	2,000L	57,60
12	MAT.SY	Syringe	18,09	1,000u	18,09
13	MAT.B	Laboratory coat	15,00	1,000u	15,00
14	MAT.SLIDE	Microscope slides	14,99	1,000u	14,99
15	MAT.STC	Double coated tape	14,00	1,000u	14,00
16	MAT.SYf	Syringe filter 0.22um pore size	12,95	1,000u	12,95
17	MAT.TIP	Micropipette tips	11,50	2,000u	23,00
18	MAT.EPP	Eppendorf tubes	8,49	1,000u	8,49
19	MAT.PFI	Parafilm	7,99	1,000u	7,99
20	MAT.G	Nitrile gloves	5,82	2,000u	11,64
21	MAT.TW	Tweezers	5,10	2,000u	10,20
22	MAT.INKtip	Inkjet printer tip	5,00	12,00h	60,00
23	MAT.H2O2	Hydrogen peroxide	2,50	1,000L	2,50
24	MAT.CAMP	Exhaust hood	2,06	10,00h	20,60
25	MAT.DY	Digital dynamometer Sauter FH 500	2,00	1,00h	2,00
26	MAT.VIAL	Glass vial	1,64	12,000u	19,68
27	MAT.N2	N2 stream	1,40	17,000m3	23,80
28	MAT.H2O	Ultrapure water	1,20	4,500L	5,63
			Total	material cost:	2.241,75

Table 6. Unit price cost table

Unitary price cost table			
Nº	Designation	Import	
		Number (Euros)	Word (Euros)
	1 Project definition		
1.1	u Labour table	71,00	SEVENTY-ONE EUROS
	2 State of the art investigation		
2.1	u State of the art	385,64	THREE HUNDRED EIGHTY-FIVE EUROS AND SIXTY-FOUR CENTS
2.2	u Learning to use programs and machinery	2.706,04	TWO THOUSAND SEVEN HUNDRED SIX EUROS AND FOUR CENTS
	3 Methodology and results		
	3.1 High accuracy single nanoparticle positioning via laser		

3.1.1	u APTES functionalization	389,55	THREE HUNDRED EIGHTY-NINE EUROS AND FIFTY-FIVE
3.1.2	u Contact angle test and nanoparticle transfer by drop casting	99,64	NINETY-NINE EUROS AND SIXTY-FOUR CENTS
3.1.3	u Nanoparticle transfer by drop casting	210,13	TWO HUNDRED TEN EUROS AND THIRTEEN CENTS
3.1.4	u Sample characterization	1.432,96	ONE THOUSAND FOUR HUNDRED THIRTY-TWO EUROS AND NINETY-SIX CENTS
3.1.5	u Positioning single nanoparticle via laser	1.494,60	ONE THOUSAND FOUR HUNDRED NINETY-FOUR EUROS AND SIXTY CENTS
	3.2 Manufacture of reconfigurable metasurface by soft lithography		
3.2.1	u Theoretical sample design and master fabrication	800,64	EIGHT HUNDRED EUROS AND SIXTY-FOUR CENTS
3.2.2	u PDMS stamp fabrication and characterization	662,68	SIX HUNDRED SIXTY-TWO EUROS AND SIXTY-EIGHT CENTS
3.2.3	u Metasurface fabrication and characterization	3.032,51	THREE THOUSAND THIRTY-TWO EUROS AND FIFTY-ONE CENTS
	3.3 Positioning of $BaTiO_3$ nanoparticles by inkjet printing		
3.3.1	u Cleaning substrate process and printing without Marks	1.149,57	ONE THOUSAND ONE HUNDRED FORTY-NINE EUROS AND FIFTY-SEVEN CENTS
3.3.2	u BaTiO3 NPs characterization	253,92	TWO HUNDRED FIFTY-THREE EUROS AND NINETY-TWO CENTS
3.3.3	u Sample with marks contact angle test	568,92	FIVE HUNDRED SIXTY-EIGHT EUROS AND NINETY-TWO CENTS
3.3.4	u Printing with marks	2.170,25	TWO THOUSAND ONE HUNDRED SEVENTY EUROS AND TEWNTY-FIVE CENTS
	3.4 Common consumables		

3.4.1	u Material fungible	1.207,94	ONE THOUSAND TWO HUNDRED AND SEVEN EUROS AND NINETY-FOUR CENTS
	4 Thesis writing and correction		
4.1	u Dissertation writing	482,10	FOUR HUNDRED EIGHTY-TWO EUROS AND TEN CENTS
4.2	u Correction of the document	792,28	SEVEN HUNDRED TWENTY-NINE EUROS AND TWENTY-EIGHT CENTS
4.3	u Exposition preparation	361,12	THREE HUNDRED SIXTY-ONE EUROS AND TWELVE CENTS

Table 7. Partial budget

ANNEXE JUSTIFICATION PRICES

Nº	Code	Ud	Description			Total
			1 Project definition			
1.1	01.01	**u**	**Labour table**			
	L.01		1,00 h	Thesis tutor distinguished researcher	30,68	30,68
	L.02		1,00 h	Thesis tutor cathedratic in photonics	30,68	30,68
	L.IBE		1,00 h	Biomedical engineer student	9,64	9,64
				Total prices per u		**71,00**
			2 State of the art investigation			
2.1	02.01	**u**	**State of the art**			
	L.IBE		40,00 h	Biomedical engineer student	9,64	385,60
	EQ.LO		40,00 h	Libre Office License	0,001	0,04
				Total prices per u		**385,64**
2.2	02.02	**u**	**Learning to use programs and machinery**			
	L.01		20,00 h	Thesis tutor distinguished researcher	30,68	613,60
	L.IBE		21,00 h	Biomedical engineer student	9,64	202,44
	EQ.RA		20,00 h	Spectrometer alpha300 (Raman-AFM) (WITEC)	45,00	900,00
	EQ.RAs		20,00 h	Software Project 4.0 (Witec)	45,00	900,00

EQ.GON		1,00 h	Goniometer Ramé-Hart	45,00	45,00
EQ.SCA		1,00 h	Software DROPImage Pro	45,00	45,00
			Total prices per u		**2.706,04**

3 Methodology and results

3.1 High accuracy single NP positioning via laser

3.1.1 03.01.01	**u**	**APTES functionalization**			
L.01		4,00 h	Thesis tutor distinguished researcher	30,68	122,72
L.IBE		4,00 h	Biomedical engineer student	9,64	38,56
EQ.US		0,50 h	Ultrasonic cleaner	45,00	22,50
EQ.ET		1,00 h	Etching: RIE ICP	90,00	90,00
MAT.ET		1,000 L	Ethanol	28,80	28,80
MAT.H2O2		1,000 L	Hydrogen peroxide	2,50	2,50
MAT.CAMP		4,00 h	Exhaust hood	2,06	8,24
MAT.N2		10,000 m3	N2 stream	1,40	14,00
MAT.H2O		1,000 L	Ultrapure water	1,25	1,25
MAT.EPP		1,000 u	Eppendorf tubes	8,49	8,49
MAT.PFI		1,000 u	Parafilm	7,99	7,99
MAT.APTES		1,000 u	APTES (3-Aminopropyl) triethoxysilane	44,50	44,50
			Total prices per u		**389,55**
3.1.2 03.01.02	**u**	**Contact angle test and NP transfer by drop casting**			
L.IBE		1,00 h	Biomedical engineer student	9,64	9,64
EQ.GON		1,00 h	Goniometer Ramé-Hart	45,00	45,00
EQ.SCA		1,00 h	Software DROPImage Pro	45,00	45,00
			Total prices per u		**99,64**
3.1.3 03.01.03	**u**	**NP transfer by drop casting**			
L.IBE		1,00 h	Biomedical engineer student	9,64	9,64
MAT.NP150		1,000 L	150 nm diameter gold spherical NPs	195,00	195,00
MAT.CAMP		1,00 h	Exhaust hood	2,06	2,06
MAT.N2		2,000 m3	N2 stream	1,40	2,80
MAT.H2O		0,500 L	Ultrapure water	1,25	0,63
			Total prices per u		**210,13**
3.1.4 03.01.04	**u**	**Sample characterization**			
L.IBE		14,00 h	Biomedical engineer student	9,64	134,96
EQ.RA		10,00 h	Spectrometer alpha300 (Raman-AFM) (WITEC)	45,00	450,00
EQ.RAs		10,00 h	Software Project 4.0 (Witec)	45,00	450,00
EQ.DFg		4,00 h	Dark field optical microscopy	90,00	360,00

	MAT.CLS		1,000 u	Clean room suit	38,00	38,00
				Total prices per u		**1.432,96**
3.1.5	03.01.05	**u**	**Positioning single NP via laser**			
	L.IBE		15,00 h	Biomedical engineer student	9,64	144,60
	EQ.RA		15,00 h	Spectrometer alpha300 (Raman-AFM) (WITEC)	45,00	675,00
	EQ.RAs		15,00 h	Software Project 4.0 (Witec)	45,00	675,00
				Total prices per u		**1.494,60**
			3.2 Manufacture of reconfigurable metasurface by soft lithography			
3.2.1	03.02.01	**u**	**Theoretical sample design and master fabrication**			
	L.IBE		2,00 h	Biomedical engineer student	9,64	19,28
	L.01		2,00 h	Thesis tutor distinguished researcher	30,68	61,36
	EQ.LIT		1,00 h	Raith 150 (lithography)	90,00	90,00
	EQ.ET		2,00 h	Etching: RIE ICP	90,00	180,00
	EQ.PVA		1,00 h	Tepla PVA (resin deposition)	90,00	90,00
	EQ.R		3,00 h	Coater EVG 101 (aluminum layer)	90,00	270,00
	EQ.RA		1,00 h	Spectrometer alpha300 (Raman-AFM) (WITEC)	45,00	45,00
	EQ.RAs		1,00 h	Software Project 4.0 (Witec)	45,00	45,00
				Total prices per u		**800,64**
3.2.2	03.02.02	**u**	**PDMS stamp fabrication and characterization**			
	L.IBE		12,00 h	Biomedical engineer student	9,64	115,68
	EQ.US		1,00 h	Ultrasonic cleaner	45,00	45,00
	MAT.MICRO		3,00 h	Optical microscope	45,00	135,00
	EQ.RA		2,00 h	Spectrometer alpha300 (Raman-AFM) (WITEC)	45,00	90,00
	EQ.RAs		2,00 h	Software Project 4.0 (Witec)	45,00	90,00
	MAT.PDMS		1,100 kg	Kit silicon Elastomer SYLGARD 184	170,00	187,00
				Total prices per u		**662,68**
3.2.3	03.02.03	**u**	**Metasurface fabrication and characterization**			
	L.IBE		27,00 h	Biomedical engineer student	9,64	260,28
	MAT.MICRO		3,00 h	Optical microscope	45,00	135,00
	EQ.RA		24,00 h	Spectrometer alpha300 (Raman-AFM) (WITEC)	45,00	1.080,00
	EQ.RAs		24,00 h	Software Project 4.0 (Witec)	45,00	1.080,00
	EQ.SEM		4,00 h	Scanning electron microscope (SEM)	45,00	180,00
	MAT.STC		1,000 u	Double coated tape	14,00	14,00
	MAT.SLIDE		1,000 u	Microscope slides	14,99	14,99
	MAT.DY		1,00 h	Digital dynamometer Sauter FH 500	2,00	2,00
	MAT.AC		0,500 L	Acetone	36,10	18,05
	MAT.PMMA		1,000 u	PMMA (Poly (methyl methacrylate))	227,00	227,00

	MAT.CAMP		4,00 h	Exhaust hood	2,06	8,24
	MAT.SYf		1,000 u	Syringe filter 0.22um pore size	12,95	12,95
				Total prices per u		**3.032,51**
				3.3 Positioning of $BaTiO_3$ NPs by inkjet printing		
3.3.1	03.03.01	**u**		**Cleaning substrate process and printing without marks**		
	L.TS		5,00 h	Technical specialist	15,66	78,30
	L.IBE		5,00 h	Biomedical engineer student	9,64	48,20
	EQ.INK		5,00 h	sciFLEXARRAYER S3 (Inkjet printer) (Scienion)	90,00	450,00
	EQ.INKs		5,00 h	Software SciFLEX_S3	90,00	450,00
	EQ.ET		0,50 h	Etching: RIE ICP	90,00	45,00
	MAT.AC		0,100 L	Acetone	36,10	3,61
	MAT.CAMP		1,00 h	Exhaust hood	2,06	2,06
	MAT.N2		5,000 m3	N2 stream	1,40	7,00
	MAT.H2O		2,000 L	Ultrapure water	1,25	2,50
	MAT.CLS		1,000 u	Clean room suit	38,00	38,00
	MAT.IPA		0,100 L	Isopropanol	49,00	4,90
	MAT.INKtip		4,00 h	PDC 90 Piezo Dispense Capillary (Inkjet printer tip)	5,00	20,00
				Total prices per u		**1.149,57**
3.3.2	03.03.02	**u**		**BaTiO3 NPs characterization**		
	L.IBE		3,00 h	Biomedical engineer student	9,64	28,92
	EQ.RA		2,00 h	Spectrometer alpha300 (Raman-AFM) (WITEC)	45,00	90,00
	EQ.RAs		2,00 h	Software Project 4.0 (Witec)	45,00	90,00
	MAT.MICRO		1,00 h	Optical microscope	45,00	45,00
				Total prices per u		**253,92**
3.3.3	03.03.03	**u**		**Sample with marks contact angle test**		
	L.IBE		3,00 h	Biomedical engineer student	9,64	28,92
	EQ.GON		2,00 h	Goniometer Ramé-Hart	45,00	90,00
	EQ.SCA		2,00 h	Software DROPImage Pro	45,00	90,00
	EQ.LIT		1,00 h	Raith 150 (lithography)	90,00	90,00
	EQ.ET		1,00 h	Etching: RIE ICP	90,00	90,00
	EQ.PVA		1,00 h	Tepla PVA (resin deposition)	90,00	90,00
	EQ.THA		1,00 h	Thermal Annealing	90,00	90,00
				Total prices per u		**568,92**
3.3.4	03.03.04	**u**		**Printing with marks**		
	L.TS		10,00 h	Technical specialist	15,66	156,60
	L.IBE		10,00 h	Biomedical engineer student	9,64	96,40
	EQ.INK		10,00 h	sciFLEXARRAYER S3 (Inkjet printer) (Scienion)	90,00	900,00

EQ.INKs		10,00 h	Software SciFLEX_S3	90,00	900,00
MAT.H2O		1,000 L	Ultrapure water	1,25	1,25
MAT.CLS		2,000 u	Clean room suit	38,00	76,00
MAT.INKtip		8,00 h	PDC 90 Piezo Dispense Capillary (Inkjet printer tip)	5,00	40,00
			Total prices per u		**2.170,25**

3.4 Common consumables

3.4.1 03.04.01	**u**	**Material fungible**			
MAT.G		2,000 u	Nitrile gloves	5,82	11,64
MAT.mPIP		2,000 u	Micropipette 0,5 - 10 uL	310,51	621,02
MAT.B		1,000 u	Laboratory coat	15,00	15,00
MAT.TIP		2,000 u	Micropipette tips	11,50	23,00
MAT.TW		2,000 u	Tweezers	5,10	10,20
MAT.SY		1,000 u	Syringe	18,09	18,09
MAT.ET		1,000 L	Ethanol	28,80	28,80
MAT.AFM		3,000 u	AFM probe	50,00	150,00
MAT.mPIP2		1,000 u	Micropipette 10-100 uL	310,51	310,51
MAT.VIAL		12,000 u	Glass vial	1,64	19,68
			Total prices per u		**1.207,94**

4 Thesis writing and correction

4.1 04.01	**u**	**Dissertation writing**			
L.IBE		50,00 h	Biomedical engineer student	9,64	482,00
EQ.LW11		50,00 h	Windows 11	0,001	0,05
EQ.LO365		50,00 h	Office 365	0,001	0,05
			Total prices per u		**482,10**
4.2 04.02	**u**	**Correction of the document**			
L.IBE		12,00 h	Biomedical engineer student	9,64	115,68
L.01		10,00 h	Thesis tutor distinguished researcher	30,68	306,80
L.02		10,00 h	Thesis tutor cathedratic in photonics	30,68	306,80
			Total prices per u		**729,28**
4.3 04.03	**u**	**Exposition preparation**			
L.IBE		12,00 h	Biomedical engineer student	9,64	115,68
L.01		4,00 h	Thesis tutor distinguished researcher	30,68	122,72
L.02		4,00 h	Thesis tutor cathedratic in photonics	30,68	122,72
			Total prices per u		**361,12**

Table 8. Contractual implementation budget

Chapter	Import
1 Project definition .	**71,00**
2 State of the art investigation .	**3.091,68**
3 Methodology and results	
3.1 High accuracy single nanoparticle positioning via laser .	3.626,88
3.2 Manufacture of reconfigurable metasurface by soft lithography .	4.495,83
3.3 Positioning of $BaTiO_3$ NPs by inkjet printing .	4.142,66
3.4 Common consumables .	1.207,94
Total 3 Methodology and results :	**13.473,31**
4 Thesis writing and correction .	**1.572,50**
Material execution budget	**18.208,49**
15% overheads	2.731,274
6% industrial profit	1.092,509
Sum	**22.032,273**
21% IVA	4.626,777
Contractual execution budget	**26.659,05**

The contracted execution budget amounts to the indicated amount of TWENTY-SIX THOUSAND SIX HUNDRED FIFTY-NINE EUROS AND FIVE CENTS.

Valencia, June 2024

Biomedical engineer
Luis Montero Barriga

CHAPTER 9. REFERENCES

1 Gric, T., & Hess, O. (2019). Chapter 5—Metasurfaces. En T. Gric & O. Hess (Eds.), Phenomena of Optical Metamaterials (pp. 131-154). Elsevier. https://doi.org/10.1016/B978-0-12-813896-0.00005-5

2 Zahra, S., Ma, L., Wang, W., Li, J., Chen, D., Liu, Y., Zhou, Y., Li, N., Huang, Y., & Wen, G. (2021). Electromagnetic metasurfaces and reconfigurable metasurfaces: A review. Frontiers in Physics, 8. https://doi.org/10.3389/fphy.2020.593411

3 Sebastian, E. M., Jain, S. K., Purohit, R., Dhakad, S. K., & Rana, R. S. (2020). Nanolithography and its current advancements. Materials Today: Proceedings, 26, 2351-2356. https://doi.org/10.1016/j.matpr.2020.02.505

4 Thompson, L. F., Willson, C. G., & Bowden, M. J. (Eds.). (1983). Introduction to microlithography: Theory, materials, and processing (Vol. 219). AMERICAN CHEMICAL SOCIETY. https://doi.org/10.1021/bk-1983-0219

5 Qin, D., Xia, Y., & Whitesides, G. M. (2010). Soft lithography for micro- and nanoscale patterning. Nature Protocols, 5(3), 491-502. https://doi.org/10.1038/nprot.2009.234

6 Nayak, L., Mohanty, S., Nayak, S. K., & Ramadoss, A. (2019). A review on inkjet printing of nanoparticle inks for flexible electronics. Journal of Materials Chemistry C, 7(29), 8771-8795. https://doi.org/10.1039/C9TC01630A

7 Brzobohatý, O., Šiler, M., Trojek, J., Chvátal, L., Karásek, V., Paták, A., Pokorná, Z., Mika, F., & Zemánek, P. (2015). Three-dimensional optical trapping of a plasmonic nanoparticle using low numerical aperture optical tweezers. Scientific Reports, 5(1), 8106. https://doi.org/10.1038/srep08106

8 Weibel, D. B., DiLuzio, W. R., & Whitesides, G. M. (2007). Microfabrication meets microbiology. Nature Reviews Microbiology, 5(3), 209-218. https://doi.org/10.1038/nrmicro1616

9 Jackman, R. J., Wilbur, J. L., & Whitesides, G. M. (1995). Fabrication of submicrometer features on curved substrates by microcontact printing. Science (New York, N.Y.), 269(5224), 664-666. https://doi.org/10.1126/science.7624795

10 Li, S., Zhang, J., He, J., Liu, W., Wang, Y., Huang, Z., Pang, H., & Chen, Y. (2023). Functional pdms elastomers: Bulk composites, surface engineering, and precision fabrication. Advanced Science, 10(34), 2304506. https://doi.org/10.1002/advs.202304506

11 Kolbow, J. D., Lindquist, N. C., Ertsgaard, C. T., Yoo, D., & Oh, S. (2021). Nano-optical tweezers: Methods and applications for trapping single molecules and nanoparticles. ChemPhysChem, 22(14), 1409-1420. https://doi.org/10.1002/cphc.202100004

12 Ren, Y., Chen, Q., He, M., Zhang, X., Qi, H., & Yan, Y. (2021). Plasmonic optical tweezers for particle manipulation: Principles, methods, and applications. ACS Nano, 15(4), 6105-6128. https://doi.org/10.1021/acsnano.1c00466

13 Scoutaris, N., Alexander, M. R., Gellert, P. R., & Roberts, C. J. (2011). Inkjet printing as a novel medicine formulation technique. Journal of Controlled Release, 156(2), 179-185. https://doi.org/10.1016/j.jconrel.2011.07.033

14 Moya, A., Gabriel, G., Villa, R., & Javier del Campo, F. (2017). Inkjet-printed electrochemical sensors. Current Opinion in Electrochemistry, 3(1), 29-39. https://doi.org/10.1016/j.coelec.2017.05.003

15 Cao, T., Yang, Z., Zhang, H., & Wang, Y. (2024). Inkjet printing quality improvement research progress: A review. Heliyon, 10(10), e30163. https://doi.org/10.1016/j.heliyon.2024.e30163

16 Ishida, N. (2024). Atomic force microscopy. En Non-Destructive Material Characterization Methods (pp. 89-125). Elsevier. https://doi.org/10.1016/B978-0-323-91150-4.00011-2

17 Horcas, I., Fernández, R., Gómez-Rodríguez, J. M., Colchero, J., Gómez-Herrero, J., & Baro, A. M. (2007). WSXM: A software for scanning probe microscopy and a tool for nanotechnology. The Review of Scientific Instruments, 78(1), 013705. https://doi.org/10.1063/1.2432410

18 Instrumentos de ciencia de superficies de Ramé-hart . (s. f.). Recuperado el 2 de julio de 2024, de https://www.ramehart.com/index.htm

19 Regueiro, A., Martí-Carrascosa, M., Torres-Cavanillas, R., & Coronado, E. (2024). Unlocking room-temperature bistable spin transition at the nanoscale: The synthesis of core@shell [Fe(NH 2 trz) 3 (NO 3) 2]@SiO 2 nanoparticles. Dalton Transactions, 53(20), 8764-8771. https://doi.org/10.1039/D4DT00911H

20 Molnár, G., Rat, S., Salmon, L., Nicolazzi, W., & Bousseksou, A. (2018). Spin crossover nanomaterials: From fundamental concepts to devices. Advanced Materials (Deerfield Beach, Fla.), 30(5). https://doi.org/10.1002/adma.201703862

21 Canet-Ferrer, J., Coronado, E., Forment-Aliaga, A., & Pinilla-Cienfuegos, E. (2014). Correction of the tip convolution effects in the imaging of nanostructures studied through scanning force microscopy. Nanotechnology, 25(39), 395703. https://doi.org/10.1088/0957-4484/25/39/395703